Article

TIR domains produce histidine-ADPR as an immune signal in bacteria

https://doi.org/10.1038/s41586-025-08930-2

Received: 27 December 2023

Accepted: 24 March 2025

Published online: 30 April 2025

Check for updates

Dziugas Sabonis[1,5], Carmel Avraham[2,5], Renee B. Chang[3,4,5], Allen Lu[3,4], Ehud Herbst[2], Arunas Silanskas[1], Deividas Vilutis[1], Azita Leavitt[2], Erez Yirmiya[2], Hunter C. Toyoda[3,4], Audrone Ruksenaite[1], Mindaugas Zaremba[1], Ilya Osterman[2], Gil Amitai[2], Philip J. Kranzusch[3,4]✉, Rotem Sorek[2]✉ & Giedre Tamulaitiene[1]✉

Toll/interleukin-1 receptor (TIR) domains are central components of pattern recognition immune proteins across all domains of life[1,2]. In bacteria and plants, TIR-domain proteins recognize pathogen invasion and then produce immune signalling molecules exclusively comprising nucleotide moieties[2–5]. Here we show that the TIR-domain protein of the type II Thoeris defence system in bacteria produces a unique signalling molecule comprising the amino acid histidine conjugated to ADP-ribose (His-ADPR). His-ADPR is generated in response to phage infection and activates the cognate Thoeris effector by binding a Macro domain located at the C terminus of the effector protein. By determining the crystal structure of a ligand-bound Macro domain, we describe the structural basis for His-ADPR and its recognition and show its role by biochemical and mutational analyses. Our analyses furthermore reveal a family of phage proteins that bind and sequester His-ADPR signalling molecules, enabling phages to evade TIR-mediated immunity. These data demonstrate diversity in bacterial TIR signalling and reveal a new class of TIR-derived immune signalling molecules that combine nucleotide and amino acid moieties.

TIR domains are conserved protein domains that are essential for innate immunity in animals, plants and bacteria[1,2]. These domains frequently form integral components of pattern recognition receptors, where their role is to initiate downstream immune signalling once infection is sensed[1,2]. It was recently shown that immune TIR domains in plants and bacteria produce nicotinamide adenine dinucleotide (NAD^+)-derived small signalling molecules that mediate the immune response, usually by inducing regulated death of the infected cell[2–5]. The extent of TIR signalling in plants and bacteria and the repertoire of TIR-produced signalling molecules are not completely understood.

Studies from the past few years have revealed the role of TIR-domain proteins in a bacterial anti-phage system called Thoeris[3,6–9]. In the Thoeris system of *Bacillus cereus* MSX-D12, TIR proteins first recognize phage infection and then convert NAD^+ to 1′′–3′ glyco-cyclic ADP-ribose molecules (1′′–3′ gcADPR, also called 3′cADPR)[3,8,9]. 1′′–3′ gcADPR binds and activates a second effector protein within the Thoeris system, called ThsA, which then depletes the cell of NAD^+ and aborts the infection process[3,9]. Some plant TIR-containing immune proteins also synthesize gcADPR isomer molecules similar to those produced by bacterial Thoeris TIRs[3,4].

Thoeris operons in bacterial genomes typically contain one or more TIR-domain proteins (ThsB), each capable of recognizing a distinct set of phages, and a single *thsA* immune effector gene[3,6]. Two main architectures, which we call here type I and type II Thoeris, have been described for bacterial Thoeris systems[3,6] (Fig. 1a). In type I systems, typified by the well-studied Thoeris of *B. cereus*, ThsA contains a C-terminal SLOG domain that specifically binds 1′′–3′ gcADPR[7,8] and an N-terminal sirtuin (SIR2) domain which is a potent NADase[3,7,10,11]. In type II Thoeris systems, the C terminus of ThsA does not comprise a SLOG domain, and instead contains a Macro domain, a domain that is known to bind ADPR derivatives[12,13] (Fig. 1a). The N terminus of ThsA in type II Thoeris comprises two transmembrane helices, similar to other bacterial immune effectors that impair the bacterial cell membrane when activated[14].

In this study, we characterized the type II Thoeris system from *Bacillus amyloliquefaciens* (also called *Bacillus velezensis*) Y2[6]. Unexpectedly, we found that the TIR protein of type II Thoeris produces His-ADPR as a signalling molecule. We show that the Macro domain of type II ThsA specifically binds the His-ADPR signalling molecule, and determine the structural basis for His-ADPR recognition by ThsA. Furthermore, we discover a family of phage proteins that specifically bind and sequester His-ADPR signals, enabling phages to overcome type II Thoeris defence.

Type I and II Thoeris use different signals

The type I Thoeris systems from *B. cereus* MSX-D12 and from *Bacillus dafuensis* FJAT-25496 both protect against phage SBSphiJ[3] (Fig. 1a). Recombinant chimeric systems expressing the ThsA from *B. cereus* (*Bc*ThsA) and the ThsB TIR protein from *B. dafuensis* (*Bd*ThsB) also defend against SBSphiJ, suggesting that TIRs from both these systems generate the same signalling molecule that activates the type I ThsA, as previously shown[3] (Fig. 1a,b).

[1]Institute of Biotechnology, Life Sciences Center, Vilnius University, Vilnius, Lithuania. [2]Department of Molecular Genetics, Weizmann Institute of Science, Rehovot, Israel. [3]Department of Microbiology, Harvard Medical School, Boston, MA, USA. [4]Department of Cancer Immunology and Virology, Dana-Farber Cancer Institute, Boston, MA, USA. [5]These authors contributed equally: Dziugas Sabonis, Carmel Avraham, Renee B. Chang. ✉e-mail: philip_kranzusch@dfci.harvard.edu; rotem.sorek@weizmann.ac.il; giedre.tamulaitiene@bti.vu.lt

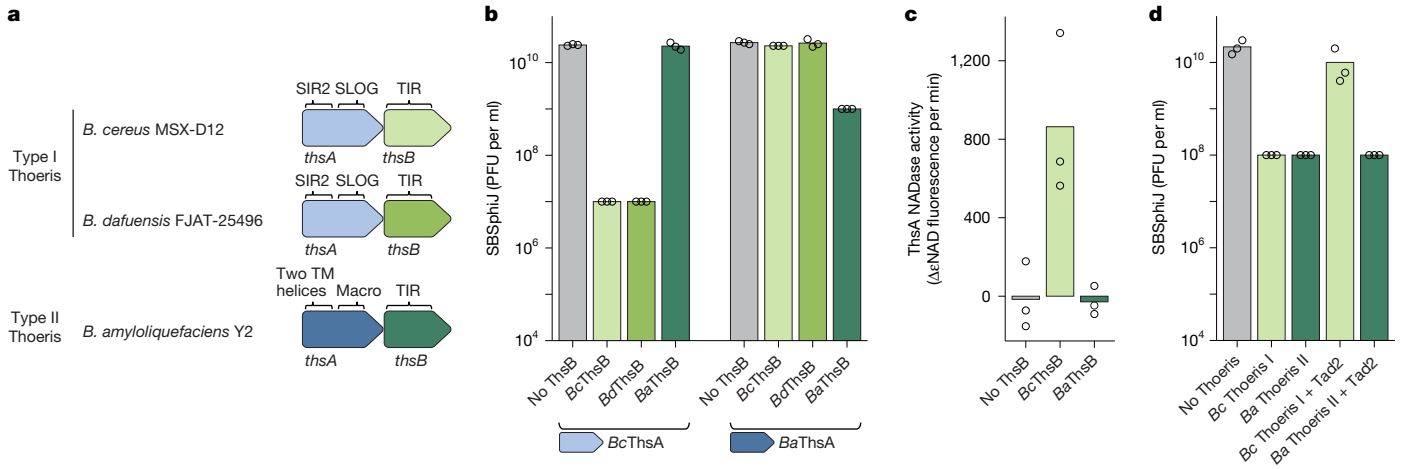

Fig. 1 | Two distinct types of Thoeris systems. a, Domain composition of the Thoeris systems studied here. TM, transmembrane. **b**, Defence phenotypes in cells expressing combinations of ThsA and ThsB proteins. Data represent titres as plaque-forming units (PFU) per ml of SBSphiJ phage infecting cells that express the indicated ThsA and ThsB combinations. ThsA is expressed from its native promoter, and ThsB is expressed from an isopropyl β-D-1-thiogalactopyranoside (IPTG)-inducible promoter. 'No ThsB' indicates control cells that express GFP instead of ThsB. **c**, Activation of *Bc*ThsA NADase activity by lysates from cells infected by phage SBSphiJ at multiplicity of infection (MOI) of 10. Infected cells express either the indicated ThsB or GFP as control (no ThsB). **d**, Tad2 inhibits type I but not type II Thoeris. Data represent titres of SBSphiJ phage infecting control cells (no Thoeris), cells expressing the type I Thoeris from *B. cereus* or type II Thoeris from *B. amyloliquefaciens*, and cells co-expressing a Thoeris system and the Tad2 protein from phage SPO1. Thoeris systems in this experiment are expressed from their native promoters. *Ba*, *B. amyloliquefaciens*; *Bc*, *B. cereus*; *Bd*, *B. dafuensis*. Bars in **b**–**d** represent an average of three replicates, with individual data points overlaid.

The type II Thoeris system from *B. amyloliquefaciens* also protects against phage SBSphiJ[6] (Fig. 1b and Extended Data Fig. 1), suggesting that the TIR protein of type II also produces a signalling molecule in response to this phage. However, we found that chimeric systems expressing the ThsA protein from type II and the TIR protein from type I Thoeris (or TIR from type II and ThsA from type I) are incapable of defending against SBSphiJ (Fig. 1b). These results suggest that the signalling molecules produced by TIRs of one type of Thoeris cannot activate the ThsA of the second type.

To further determine whether TIRs from types I and II Thoeris systems produce similar or different molecules, we experimented with cells expressing the TIR-domain protein alone, without the presence of the effector ThsA. We infected these cells with phage SBSphiJ and then lysed the cells and filtered the lysates to enrich for small molecules. As expected, purified *Bc*ThsA (from type I Thoeris) incubated with filtered cell lysates derived from infected cells expressing *B. cereus* TIR (*Bc*ThsB) exhibited strong NADase activity, confirming that the *Bc*ThsB protein from type I Thoeris produced 1′′–3′ gcADPR in response to SBSphiJ infection, as previously demonstrated[15] (Fig. 1c). However, filtered cell lysates derived from cells expressing the TIR from type II Thoeris (*B. amyloliquefaciens* TIR (*Ba*ThsB)) were not able to activate *Bc*ThsA in vitro, confirming that the TIR protein of type II Thoeris does not produce a molecule capable of activating the ThsA from type I Thoeris.

A recent study reported that some phages encode an anti-Thoeris protein called Tad2 (Thoeris anti-defence 2), which binds and sequesters the 1′′–3′ gcADPR signalling molecule produced by Thoeris TIRs[15]. Tad2 forms a homotetrameric complex containing two pockets that bind gcADPR molecules with low nanomolar affinity[15]. We co-expressed the type I Thoeris system with the Tad2 protein from phage SPO1, and found that Tad2 blocks Thoeris defence, as expected (Fig. 1d). However, Tad2 did not abolish defence when co-expressed with type II Thoeris, further indicating that the type II system does not rely on the production of 1′′–3′ gcADPR molecules. As Tad2 is also known to bind and sequester the related molecule 1′′–2′ gcADPR[9], our data suggest that the TIR protein of type II Thoeris generates neither 1′′–3′ gcADPR nor 1′′–2′ gcADPR.

A phage protein sequesters type II signal

Phylogenetic analyses of the Tad2 protein family revealed that homologues of this protein are encoded by phages infecting a large variety of bacteria spanning multiple phyla[15]. Most of the Tad2 homologues that were previously tested experimentally were able to inhibit type I Thoeris, suggesting that they bind the 1′′–3′ gcADPR signalling molecule[15] (Fig. 2a). However, one Tad2 homologue, encoded by a prophage of *Myroides odoratus*, did not abolish anti-phage defence when co-expressed with the type I Thoeris system[15] (Fig. 2a,b). We hypothesized that the Tad2 from *M. odoratus* (*Mo*Tad2) evolved to recognize and sequester the signalling molecule of type II Thoeris. In support of this hypothesis, co-expression of *Mo*Tad2 with the type II Thoeris from *B. amyloliquefaciens* rendered this system unable to protect against phage SBSphiJ. Close homologues of *Mo*Tad2 from prophages of *Clostridium cadaveris* (*Cc*Tad2) and *Tatumella morbirosei* (*Tm*Tad2) were also capable of inhibiting type II Thoeris, suggesting that the clade of proteins represented by *Mo*Tad2 and its homologues can bind the molecule produced by the type II Thoeris TIR (Fig. 2a–c and Extended Data Fig. 2).

To gain further insight into the nature of the signalling molecule produced by the type II Thoeris TIR in response to infection, we used *Mo*Tad2 as a 'sponge' to bind this molecule. We incubated *Mo*Tad2 with filtered lysates derived from phage-infected cells expressing *Ba*ThsB, washed the *Mo*Tad2 complexes by successive dilution and concentration, and heated the ligand-bound *Mo*Tad2 at 98 °C to denature the protein and release the signalling molecule (Fig. 2d). Metabolomic analysis using untargeted mass spectrometry revealed a unique mass with a retention time of 9.04 min and an m/z value of 697.1374 (positive ionization mode) that was present in the sample retrieved from the denatured *Mo*Tad2 (Fig. 2d). This mass was also present in filtered cell lysates prior to exposure to *Mo*Tad2, and was eliminated from these lysates following exposure to *Mo*Tad2, indicating that *Mo*Tad2 specifically binds and sequesters this molecule (Fig. 2d). The unique molecule could not be detected in lysates derived from control cells expressing green fluorescent protein (GFP) instead of *Ba*ThsB (Fig. 2d and Extended Data Fig. 3), and was furthermore undetectable in non-infected cells

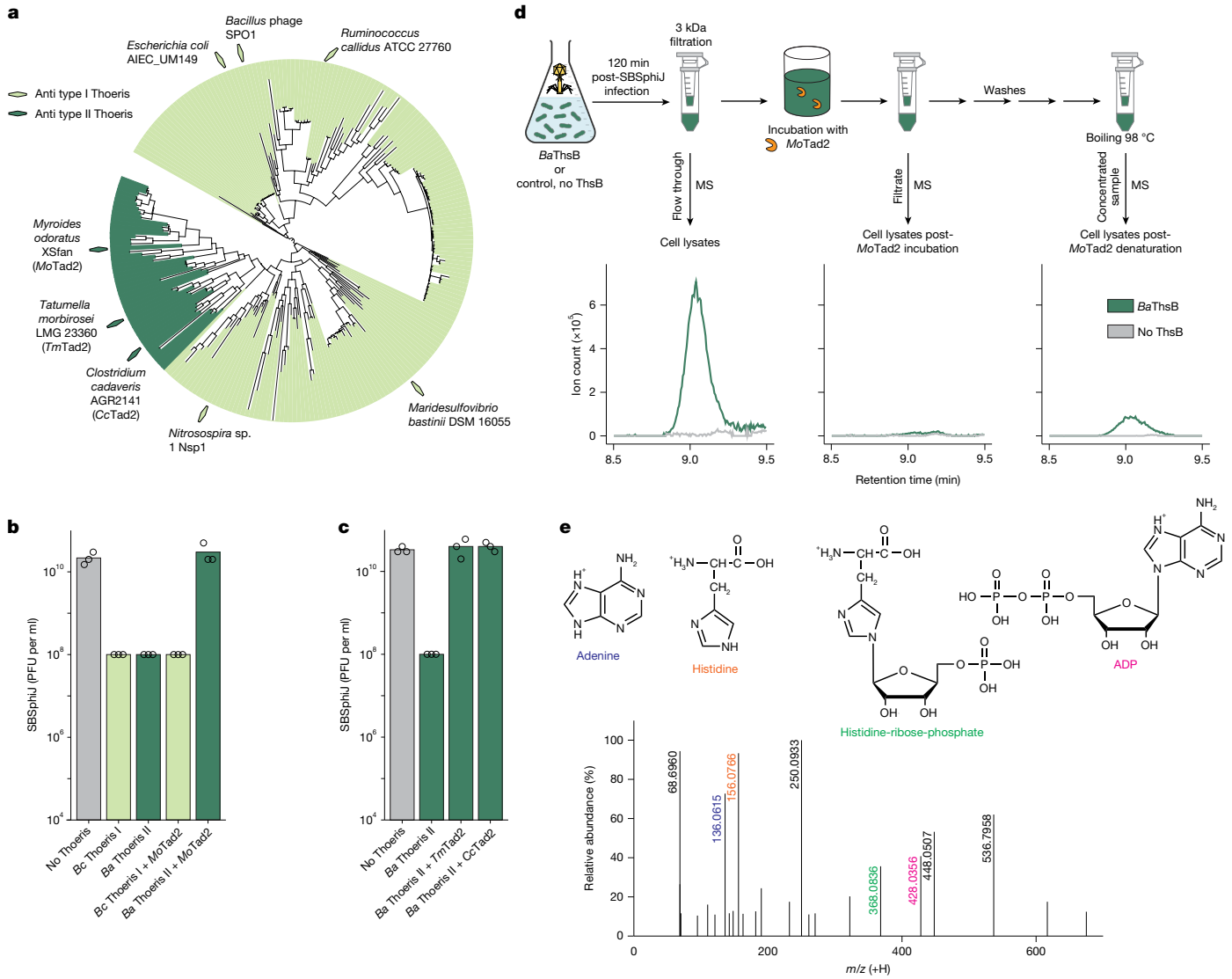

Fig. 2 | A phage protein that binds and sequesters the signalling molecule of type II Thoeris. a, Phylogenetic analysis of Tad2 homologues in phage and prophage genomes. The names of bacteria and phages from which Tad2 homologues were previously tested and found to inhibit type I Thoeris[15] are indicated on the tree by light green diamonds. Names of Tad2 homologues found to inhibit type II Thoeris in the current study are indicated by dark green diamonds. Structure of the presented tree is as described[15]. **b**, *Mo*Tad2 inhibits type II Thoeris but not type I Thoeris. **c**, *Tm*Tad2 and *Cc*Tad2 inhibit type II Thoeris. Data in **b**,**c** represent titres of SBSphiJ phage infecting bacterial cells and bars show an average of three replicates with individual data points overlaid. **d**, *Mo*Tad2 binds a small-molecule ligand. Cells expressing *Ba*ThsB or control cells that express GFP instead were infected with phage SBSphiJ at a MOI of 10. After 120 min the cells were lysed, lysates were filtered, and then lysates were incubated with purified *Mo*Tad2. The lysates before and after incubation with *Mo*Tad2, or after denaturation of *Mo*Tad2, were analysed by mass spectrometry (MS). Extracted mass chromatograms of ions with an *m*/*z* value of 697.1374 and retention time of 9.04 min in positive mode are presented. Data are representative of two replicates; full replicate data are presented in Extended Data Fig. 3. **e**, MS/MS fragmentation spectra of the type II Thoeris-derived molecule. Hypothesized structures of selected MS/MS fragments are presented. The presented MS/MS data were obtained in positive ionization mode for the filtrate after *Mo*Tad2 denaturation.

(Extended Data Fig. 4), suggesting that this molecule is specifically produced by *Ba*ThsB.

Tandem mass spectrometry (MS/MS) analysis of the molecule released by *Mo*Tad2 revealed fragments with *m*/*z* values of adenine and ADP, suggesting that the molecule may be related to ADPR (Fig. 2e). In addition to these fragments, however, we detected an abundant fragment with an *m*/*z* value of 156.0766, which, when compared to common cellular metabolites, unexpectedly revealed a perfect match to the amino acid histidine. Another abundant fragment ion exhibited an *m*/*z* value matching the expected mass of histidine-ribose-phosphate (Fig. 2e). These data suggested that the signalling molecule involves derivatives of both adenine nucleotide and histidine (Fig. 2e).

ThsA Macro domain pocket binds His-ADPR

In the type II Thoeris system, the ThsA protein effector has a C-terminal Macro domain, which is predicted to bind the signalling molecule derived from the respective TIR protein (Fig. 1a). To gain further insight into the new signalling molecule, we co-expressed *Ba*ThsB with the Macro domain of *B. amyloliquefaciens* ThsA (*Ba*ThsA) (residues 83–297, *Ba*Macro), and found that it co-purifies with a ligand having a mass identical (within the expected measurement error) to the mass of the molecule we identified bound to *Mo*Tad2 (Extended Data Fig. 5a). No molecule co-purified with the *Ba*Macro protein when co-expressed with *B. amyloliquefaciens* ThsB (*Ba*ThsB) catalytic mutant E99A (Extended Data Fig. 5a). We then determined a crystal structure of *Ba*Macro bound

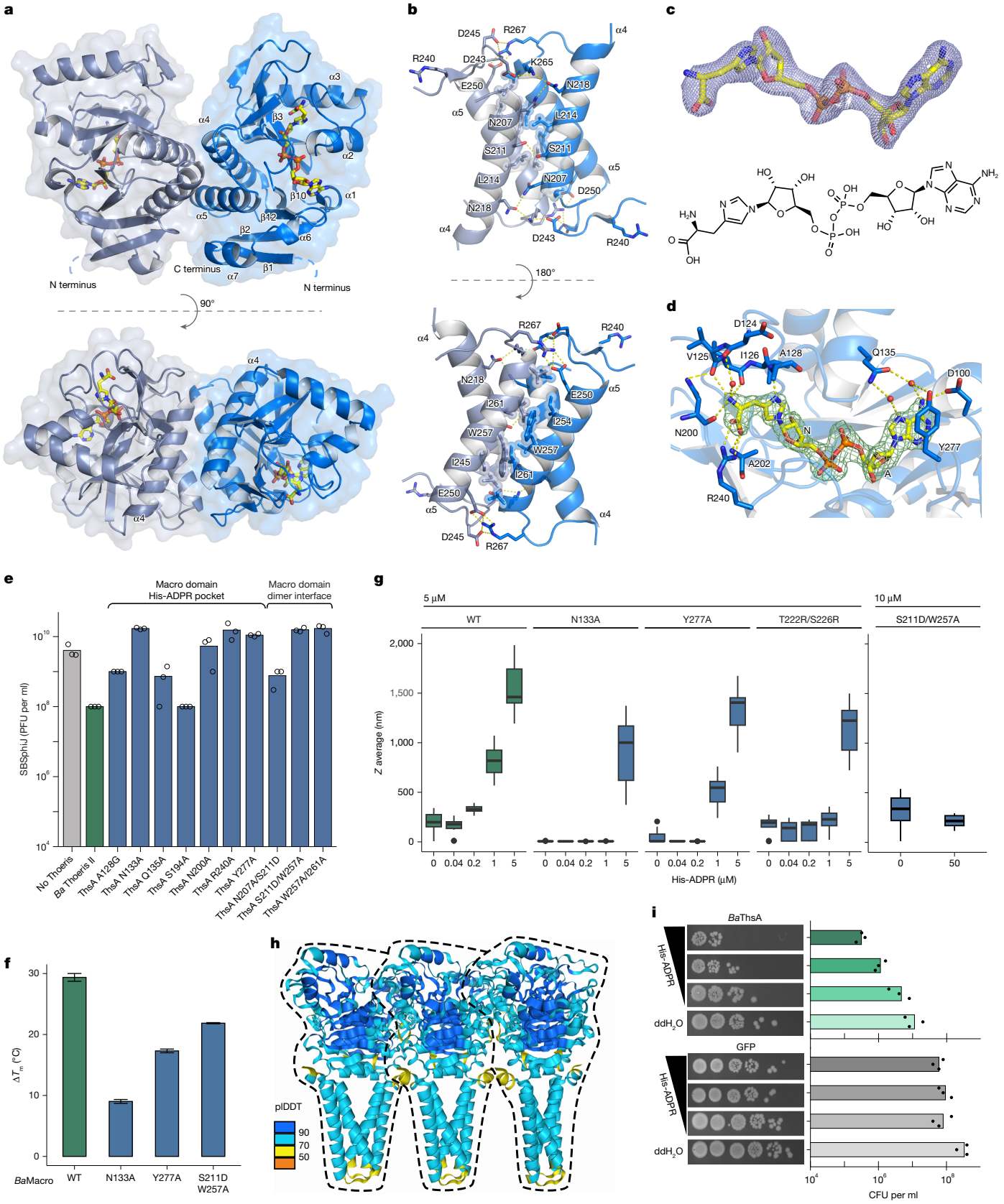

Fig. 3 | See next page for caption.

to the ligand molecule at 2.23 Å resolution (Fig. 3a). We found that the *Ba*Macro domain of type II Thoeris forms a homodimeric complex, with each protomer possessing a globular α/β/α sandwich fold typical to Macro domain structures, composed of a central seven-stranded mixed β sheet (β1–β2–β12–β10–β3–β7–β6) flanked by seven α helices (Extended Data Fig. 5b). Dali structure comparison[16] revealed that

Fig. 3 | Structure of *Ba*Macro bound to His-ADPR. a, *Ba*Macro dimer structure. Protomers are depicted in different colours, His-ADPR is shown in yellow. **b**, Dimerization interface of the *Ba*Macro domain. **c**, Polder omit map of the ligand-binding site contoured at 5σ, showing the chemical structure of the ligand to be His-ADPR. **d**, Detailed view of the *Ba*Macro residues interacting with the adenine base and histidine moiety of His-ADPR. Yellow dashed lines denote hydrogen-bonding interactions. A and N mark A-ribose and N-ribose, respectively. Light green mesh denotes $2F_o - F_c$ electron density of His-ADPR contoured at 1.5σ. A full view of the interactions of *Ba*Macro with His-ADPR is presented in Extended Data Fig. 5e. **e**, Results of phage infection experiments with wild-type *Ba*ThsA, and His-ADPR pocket and dimer interface mutants. Cells express either the wild-type *Ba* Thoeris system, or a Thoeris system in which ThsA contains the indicated point mutation. **f**, Protein melting data showing difference in T_m between apo *Ba*Macro and His-ADPR-bound domain and its mutants. Bars represent the independent experiment difference of the averaged $n = 3$ technical replicates ± difference s.d. (Methods). WT, wild type. **g**, Dynamic light scattering data showing His-ADPR-dependent oligomerization of the *Ba*Macro domain and its mutants. No oligomerization was detected for the S211D/W257A mutant. Data ($n = 10$ measurements each) are represented as box plots. The box bounds the interquartile range with the horizontal line representing the median; whiskers extend to a maximum of 1.5 times the interquartile range beyond the box. **h**, AlphaFold 3 model prediction of six *Ba*ThsA protomers. Residues are coloured by plDDT score. The interface predicted template modelling (ipTM) score is 0.76. **i**, Survivability spot assay of *E. coli* carrying *Ba*ThsA or GFP genes, incubated in the presence of various His-ADPR concentrations. In **e**,**i**, bars represent the average of $n = 3$ replicates (representative shown in **i**) with individual data points overlaid.

*Ba*Macro exhibits similarity to an ADPribosyl hydrolase MacroD-like domain from the bacterium *Oceanobacillus iheyensis* and to a catalytically inactive MacroH2A-like domain from the amoeboid protist *Capsaspora owczarzaki*[13,17,18] (Extended Data Fig. 5c). Comparing *Ba*Macro to these structures, we found that the loops near the ligand-binding pocket are longer in *Ba*Macro and possess an additional β hairpin (strands β4 and β5) and a small additional β-sheet (strands β8, β9 and β11). In the ligand-binding pocket the adenine binding residues are conserved, but the MacroD-type catalytic aspartate is absent in *Ba*Macro (Extended Data Fig. 5d). Although Macro domains are generally known to be monomeric[13,19], *Ba*Macro forms a dimer in the crystal with a substantial dimer interface of approximately 960 Å^2 involving helices α4 and α5 (Fig. 3b).

Further examining the predicted ligand-binding region in *Ba*Macro, we found that each *Ba*Macro protomer has a ligand molecule bound in a deep elongated conserved binding pocket (Fig. 3a). Clear electron density in the binding pocket, as well as a hydrogen-bonding network with the protein, enabled us to identify the ligand bound in the *Ba*Macro domain pocket as a histidine that was covalently linked to ADPR (termed here His-ADPR) (Fig. 3c,d and Extended Data Fig. 5e). In this molecule, the histidine forms a β-glycosidic bond to the C1′ atom of ADPR N-ribose through its side chain NE1 (τ) atom (Fig. 3c). The theoretical relative molecular mass of His-ADPR in the protonated form (697.1379) is within the expected measurement error of the mass of the molecule we identified bound to *Mo*Tad2 (697.1374), and the MS/MS fragments determined for the *Mo*Tad2-derived molecule match the His-ADPR structure (Fig. 2e).

Further analysis of the His-ADPR-binding site demonstrated that the *Ba*Macro domain makes many contacts (around 30 hydrogen bonds) with the His-ADPR ligand (Fig. 3d and Extended Data Fig. 5e). Binding of the adenine moiety is conserved with other Macro domains, involving stacking interaction with Y277 and a hydrogen bond between D100 and N6 of the adenine base[13,17] (Extended Data Fig. 5d, e). The A-ribose and diphosphate of His-ADPR are bound mostly by protein backbone atoms, and the side chains of N133 and S194 (Extended Data Fig. 5e). The histidine moiety of the His-ADPR ligand is bound by main chain atoms of *Ba*Macro, and by residue R240 of *Ba*Macro. Mutations of the Macro domain residues involved in His-ADPR binding and dimer interface abolished the anti-phage activity of type II Thoeris without having an effect on the expression of the protein (Fig. 3e and Extended Data Fig. 5f).

His-ADPR induces *Ba*Macro oligomerization

To test whether type II ThsB proteins are able to synthesize His-ADPR in vitro we purified a set of the type II ThsB homologues and incubated them with NAD$^+$ and free histidine. In vitro synthesis of His-ADPR was observed in the case of the *Ba*ThsB and its homologue *Eubacterium rectale* (ATCC 33656) *Er*ThsB (61% amino acid sequence identity to *Ba*ThsB) (Extended Data Fig. 6a). The yield of His-ADPR synthesis was low, probably because the unknown phage-derived signal that activates type II Thoeris was not present in the in vitro system. Such low-level in vitro production of signalling molecule was also observed for the type I Thoeris protein ThsB′ from *B. cereus* MSX-D12[20]. Therefore, for further biochemical studies, the His-ADPR molecule was obtained from the *Ba*Macro preparation, when it was co-expressed with *Ba*ThsB, by denaturing the protein and purifying His-ADPR by high-performance liquid chromatography (HPLC) (Extended Data Fig. 6b).

To gain further insights into the effect of the His-ADPR binding, we purified apo *Ba*Macro domain expressed without *Ba*ThsB. Size-exclusion chromatography with multi-angle light scattering (SEC-MALS) data indicate that apo *Ba*Macro forms a dimer in solution (Extended Data Fig. 7a). Thermal shift assay showed that His-ADPR binding substantially increased melting temperature (T_m) of *Ba*Macro by around 30 °C (Fig. 3f). Moreover, we found that addition of His-ADPR caused oligomerization of *Ba*Macro, as observed by dynamic light scattering (Fig. 3g). Oligomerization of the Macro domains is consistent with the AlphaFold 3 model[21] of *Ba*ThsA with predicted oligomerization through the Macro domains (Fig. 3h). Mutations in the ligand-binding pocket (N133A and Y277A) markedly reduced thermal stabilization and domain oligomerization induced by His-ADPR binding (Fig. 3f,g and Extended Data Fig. 7a). Mutations at the Macro domain dimer interface (S211D/W257A) and predicted oligomerization interface (T222R/S226R) had a smaller influence on His-ADPR binding thermal shift but they had destabilizing effect on the dimer and prevented or weakened oligomer formation induced by His-ADPR binding, respectively (Fig. 3f,g and Extended Data Fig. 7).

To directly determine whether ThsA is activated by His-ADPR to inflict a toxic effect on the cell, we incubated *Escherichia coli* cells expressing *Ba*ThsA in a medium supplemented with His-ADPR. The growth of *Ba*ThsA-expressing cells was substantially impaired in the presence of 0.5–1.0 mM His-ADPR, but no effect was observed when cells expressing GFP were exposed to His-ADPR (Fig. 3i). Together, these experiments show that His-ADPR is the signalling molecule of type II Thoeris system.

Structure of *Mo*Tad2 bound to His-ADPR

To define the molecular mechanism of type II Thoeris evasion by *Mo*Tad2, we determined crystal structures of *Mo*Tad2 in the apo and His-ADPR ligand-bound states (Fig. 4a and Extended Data Fig. 8a). *Mo*Tad2 is a tetramer formed by two V-shaped homodimers that exhibit a similar overall architecture to *Bacillus* phage SPO1 Tad2, which binds the signalling molecule 1′′–3′ gcADPR (gcADPR) and inhibits type I Thoeris defence[15] (Extended Data Fig. 8a). A 1.67 Å crystal structure revealed that *Mo*Tad2 forms a complex with His-ADPR, confirming our hypothesis that *Mo*Tad2 evades type II Thoeris defence by sequestering the immune signalling molecule His-ADPR (Fig. 4a). Notably, *Mo*Tad2 sequesters His-ADPR in two symmetric pockets that share structural homology with the gcADPR binding pocket of SPO1 Tad2 (Fig. 4a,b and Extended Data Fig. 8b). Each homodimer of the *Mo*Tad2 complex sequesters a single molecule of His-ADPR, and the dimeric units (denoted *Mo*Tad2$_A$–*Mo*Tad2$_B$ and *Mo*Tad2$_C$–*Mo*Tad2$_D$) interlock

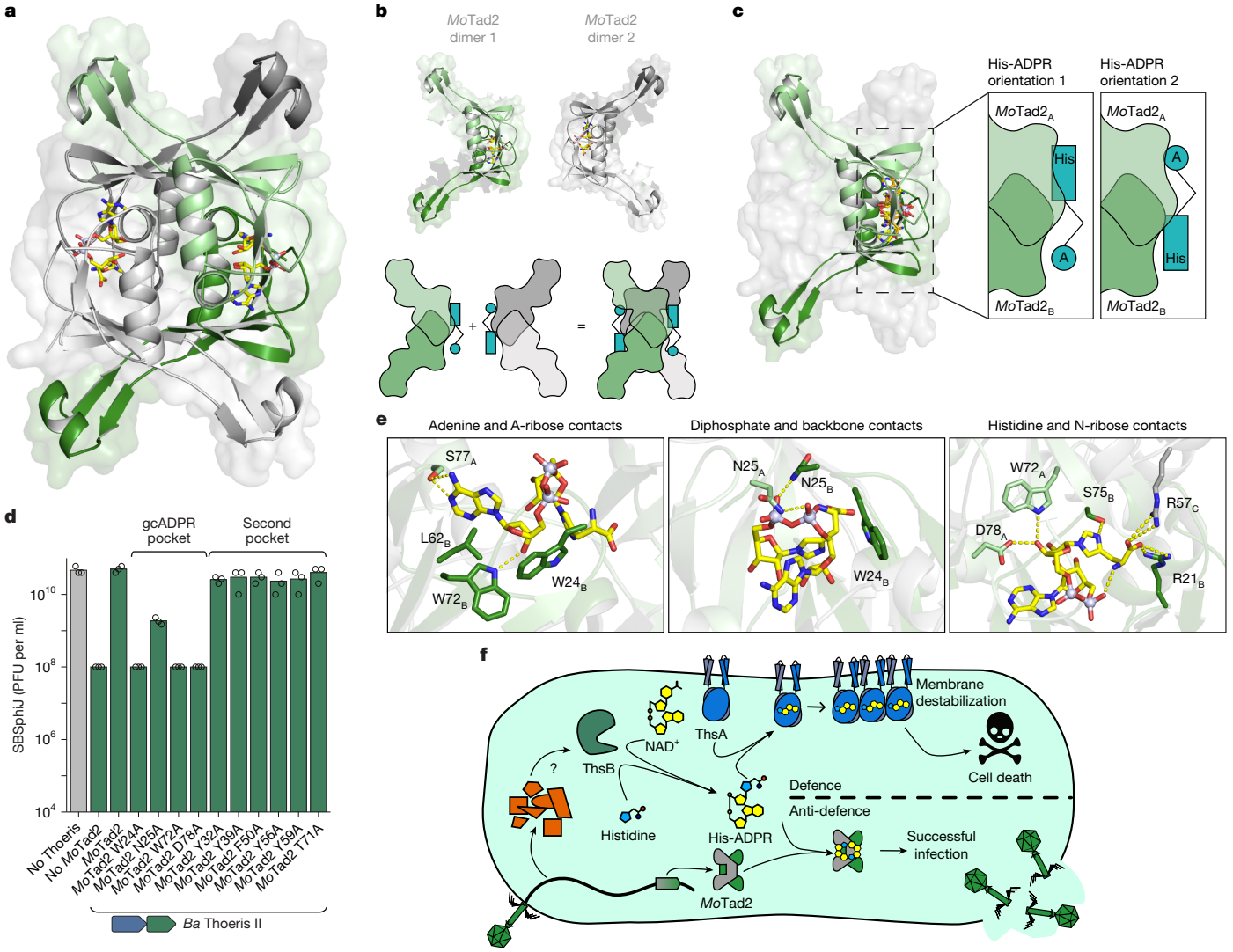

Fig. 4 | Structural basis of His-ADPR sequestration by *Mo*Tad2. a, *Mo*Tad2–His-ADPR complex structure. Protomers are depicted in different colours, His-ADPR is shown in yellow. **b**, Schematic representation of *Mo*Tad2 tetramer. **c**, His-ADPR is bound in two orientations in the symmetric pocket. **d**, Results of phage infection experiments of the *Mo*Tad2 pockets. Cells express wild-type *Ba* Thoeris and either wild-type *Mo*Tad2 or *Mo*Tad2 with the indicated point mutation. Bars represent an average of three replicates, with individual data points overlaid. **e**, Specific contacts to His-ADPR in the pocket. **f**, Model for the mechanism of action of type II Thoeris.

to form a compact tetrameric assembly (Fig. 4b). The His-ADPR-binding pocket is located at the interface between helix α3 and the β5–β6 loop region of two *Mo*Tad2 protomers from the same dimeric unit, and we observed His-ADPR binding in two orientations (Fig. 4b,c). Mutagenesis of residues in the His-ADPR pocket of *Mo*Tad2 (equivalent to the gcADPR pocket of SPO1 Tad2) abrogated evasion of type II Thoeris defence in vivo, suggesting that *Mo*Tad2 specifically evolved to recognize His-ADPR (Fig. 4d). Mutations in a second potential pocket that was recently shown to bind other immune signalling molecules did not affect the ability of *Mo*Tad2 to evade type II Thoeris defence[22], further supporting that His-ADPR is uniquely bound in the form identified by the crystal structure (Fig. 4d and Extended Data Fig. 8c).

Several features in the *Mo*Tad2$_A$–*Mo*Tad2$_B$ binding pocket interface enable selective recognition of His-ADPR via a series of nucleobase-, sugar- and backbone-specific contacts. The adenine base of His-ADPR is coordinated by hydrogen bonds from *Mo*Tad2$_A$ S77 to N1 and N6 on the nucleobase Watson–Crick edge and van der Waals contacts from *Mo*Tad2$_B$ L62 (Fig. 4e). The A-ribose forms contacts with W72 and van der Waals interactions with W24 of *Mo*Tad2$_B$ (Fig. 4e). Additional polar contacts with the backbone of His-ADPR secure the molecule within the binding pocket, with residues N25 of *Mo*Tad2$_A$ and N25 of *Mo*Tad2$_B$ forming hydrogen bonds with the carbonyl and hydroxyl oxygen of the diphosphate group, respectively (Fig. 4e). The histidine moiety of His-ADPR is anchored by an extensive network of hydrogen bonds from *Mo*Tad2$_B$S75 and R21, and R57 of *Mo*Tad2$_C$ from the opposite dimeric unit (Fig. 4e). Similarly, the N-ribose of His-ADPR is bound by polar interactions from *Mo*Tad2$_A$ W72 and D78 with the 3′ hydroxyl group (Fig. 4e). Together, our results explain the structural basis by which *Mo*Tad2 inhibits type II Thoeris defence by sequestering His-ADPR, thereby preventing the activation of downstream Thoeris effector proteins.

Discussion

Our study establishes His-ADPR as the immune signalling molecule produced by the type II Thoeris defence system. This molecule represents a new class of TIR-derived immune signalling molecules comprising an amino acid conjugated to the nucleotide ADPR. Prior to the current study, immune TIR-domain proteins in plants and bacteria were shown to produce exclusively nucleotide-based signalling molecules, in which ADPR was either cyclized[4,8,9] or conjugated to another nucleotide[23]. In other

cases, TIR domains were shown to produce nucleotide-based signals by processing the ends of DNA and RNA[24]. Our discovery raises the possibility that nucleotide–amino acid conjugates may serve as TIR-derived second messengers in other TIR-dependent defence systems.

Our data show that the His-ADPR molecule is produced by type II Thoeris ThsB in response to phage infection. We propose that His-ADPR synthesis is carried out via a double-displacement mechanism in analogy to SARM1 TIR domain[25] (Extended Data Fig. 9). Then His-ADPR is bound by the Macro domain of ThsA and induces its oligomerization (Fig. 4f). The ThsA oligomer formation destabilizes the cell membrane and induces cell death. We further show that phages can escape type II Thoeris defence by sequestering His-ADPR using the phage-encoded *Mo*Tad2 sponge protein.

Defence systems that rely on second messenger signalling are abundant in bacteria and have been detected in at least 20% of sequenced bacterial and archaeal genomes[26]. In addition to Thoeris, these systems include cyclic-oligonucleotide-based anti-phage signalling system (CBASS)[27–29], Pycsar[30] and type III CRISPR–Cas[31,32]. All these systems generate nucleotide-centric signalling molecules, with each system employing distinct enzymatic biochemistry for signal production: nucleotide polymerization in the case of CBASS and type III CRISPR systems, mononucleotide cyclization in Pycsar systems, and TIR-mediated NAD^+ processing for Thoeris[33]. Notably, a recent study identified a version of type III CRISPR–Cas that utilizes the nucleotide polymerization biochemistry of Cas10 to conjugate *S*-adenosyl methionine (SAM) to ATP, generating a SAM-AMP immune signalling molecule[34]. Together with the results of our study, these data demonstrate that enzymes producing immune signalling molecules can evolve to incorporate non-nucleotide moieties within the produced signal. As phages express nuclease and sponge proteins that degrade and sequester specific immune signalling molecules[9,15,35–38], this generates a strong evolutionary pressure for signal diversification in bacterial defence systems.

For many years, TIR domains were known only as protein–protein interaction modules[39], and the NADase activity of TIR domains was discovered relatively recently[40–42]. TIR-mediated small-molecule signalling in immunity is a more recent discovery[8,9]. So far, TIRs in plants and bacteria have been shown to produce diverse molecules including gcADPR[8,9], 2′-(5″-phosphoribosyl)-AMP/ADP (Rib-AMP/ADP)[43], ADPR–ADPR[23], ADPR-ATP[23], ADP-cyclo[N7:1″]-ribose (N7-cADPR)[44] and now His-ADPR. Together, these discoveries demonstrate remarkable plasticity in the ability of TIR domains to produce signalling molecules via conjugation of ADPR and suggest that more TIR-produced signalling molecules may be identified in the future.

Online content

Any methods, additional references, Nature Portfolio reporting summaries, source data, extended data, supplementary information, acknowledgements, peer review information; details of author contributions and competing interests; and statements of data and code availability are available at https://doi.org/10.1038/s41586-025-08930-2.

1. Fitzgerald, K. A. & Kagan, J. C. Toll-like receptors and the control of immunity. *Cell* **180**, 1044–1066 (2020).
2. Essuman, K., Milbrandt, J., Dangl, J. L. & Nishimura, M. T. Shared TIR enzymatic functions regulate cell death and immunity across the tree of life. *Science* **377**, eabo0001 (2022).
3. Ofir, G. et al. Antiviral activity of bacterial TIR domains via immune signalling molecules. *Nature* **600**, 116–120 (2021).
4. Bayless, A. M. et al. Plant and prokaryotic TIR domains generate distinct cyclic ADPR NADase products. *Sci. Adv.* **9**, eade8487–eade8487 (2023).
5. Li, S., Manik, M. K., Shi, Y., Kobe, B. & Ve, T. Toll/interleukin-1 receptor domains in bacterial and plant immunity. *Curr. Opin. Microbiol.* **74**, 102316 (2023).
6. Doron, S. et al. Systematic discovery of antiphage defense systems in the microbial pangenome. *Science* **359**, eaar4120 (2018).
7. Ka, D., Oh, H., Park, E., Kim, J.-H. & Bae, E. Structural and functional evidence of bacterial antiphage protection by Thoeris defense system via NAD^+ degradation. *Nat. Commun.* **11**, 2816 (2020).
8. Manik, M. K. et al. Cyclic ADP ribose isomers: production, chemical structures, and immune signaling. *Science* **377**, eadc8969 (2022).
9. Leavitt, A. et al. Viruses inhibit TIR gcADPR signalling to overcome bacterial defence. *Nature* **611**, 326–331 (2022).
10. Garb, J. et al. Multiple phage resistance systems inhibit infection via SIR2-dependent NAD^+ depletion. *Nat. Microbiol.* **7**, 1849–1856 (2022).
11. Zaremba, M. et al. Short prokaryotic Argonautes provide defence against incoming mobile genetic elements through NAD^+ depletion. *Nat. Microbiol.* **7**, 1857–1869 (2022).
12. Karras, G. I. et al. The macro domain is an ADP-ribose binding module. *EMBO J.* **24**, 1911–1920 (2005).
13. Rack, J. G. M., Perina, D. & Ahel, I. Macrodomains: structure, function, evolution, and catalytic activities. *Annu. Rev. Biochem.* **85**, 431–454 (2016).
14. Duncan-Lowey, B., McNamara-Bordewick, N. K., Tal, N., Sorek, R. & Kranzusch, P. J. Effector-mediated membrane disruption controls cell death in CBASS antiphage defense. *Mol. Cell* **81**, 5039–5051.e5 (2021).
15. Yirmiya, E. et al. Phages overcome bacterial immunity via diverse anti-defence proteins. *Nature* **625**, 352–359 (2023).
16. Holm, L. Dali server: structural unification of protein families. *Nucleic Acids Res.* **50**, W210–W215 (2022).
17. Zapata-Pérez, R. et al. Structural and functional analysis of *Oceanobacillus iheyensis* macrodomain reveals a network of waters involved in substrate binding and catalysis. *Open Biol.* **7**, 160327 (2017).
18. Guberovic, I. et al. Evolution of a histone variant involved in compartmental regulation of NAD metabolism. *Nat. Struct. Mol. Biol.* **28**, 1009–1019 (2021).
19. Rack, J. G. M., Palazzo, L. & Ahel, I. (ADP-ribosyl)hydrolases: structure, function, and biology. *Genes Dev.* **34**, 263–284 (2020).
20. Tamulaitiene, G. et al. Activation of Thoeris antiviral system via SIR2 effector filament assembly. *Nature* **627**, 431–436 (2024).
21. Abramson, J. et al. Accurate structure prediction of biomolecular interactions with AlphaFold 3. *Nature* **630**, 493–500 (2024).
22. Li, D. et al. Single phage proteins sequester signals from TIR and cGAS-like enzymes. *Nature* **635**, 719–727 (2024).
23. Jia, A. et al. TIR-catalyzed ADP-ribosylation reactions produce signaling molecules for plant immunity. *Science* **377**, eabq8180 (2022).
24. Yu, D. et al. TIR domains of plant immune receptors are 2′,3′-cAMP/cGMP synthetases mediating cell death. *Cell* **185**, 2370–2386.e18 (2022).
25. Shi, Y. et al. Structural basis of SARM1 activation, substrate recognition, and inhibition by small molecules. *Mol. Cell* **82**, 1643–1659.e10 (2022).
26. Tesson, F. et al. Systematic and quantitative view of the antiviral arsenal of prokaryotes. *Nat. Commun.* **13**, 2561 (2022).
27. Cohen, D. et al. Cyclic GMP–AMP signalling protects bacteria against viral infection. *Nature* **574**, 691–695 (2019).
28. Whiteley, A. T. et al. Bacterial cGAS-like enzymes synthesize diverse nucleotide signals. *Nature* **567**, 194–199 (2019).
29. Duncan-Lowey, B. & Kranzusch, P. J. CBASS phage defense and evolution of antiviral nucleotide signaling. *Curr. Opin. Immunol.* **74**, 156–163 (2022).
30. Tal, N. et al. Cyclic CMP and cyclic UMP mediate bacterial immunity against phages. *Cell* **184**, 5728–5739.e16 (2021).
31. Niewoehner, O. et al. Type III CRISPR–Cas systems produce cyclic oligoadenylate second messengers. *Nature* **548**, 543–548 (2017).
32. Kazlauskiene, M., Kostiuk, G., Venclovas, Č., Tamulaitis, G. & Siksnys, V. A cyclic oligonucleotide signaling pathway in type III CRISPR–Cas systems. *Science* **357**, 605–609 (2017).
33. Athukoralage, J. S. & White, M. F. Cyclic nucleotide signaling in phage defense and counter-defense. *Annu. Rev. Virol.* **9**, 451–468 (2022).
34. Chi, H. et al. Antiviral type III CRISPR signalling via conjugation of ATP and SAM. *Nature* **622**, 826–833 (2023).
35. Hobbs, S. J. et al. Phage anti-CBASS and anti-Pycsar nucleases subvert bacterial immunity. *Nature* **605**, 522–526 (2022).
36. Athukoralage, J. S. et al. An anti-CRISPR viral ring nuclease subverts type III CRISPR immunity. *Nature* **577**, 572–575 (2020).
37. Huiting, E. et al. Bacteriophages inhibit and evade cGAS-like immune function in bacteria. *Cell* **186**, 864–876.e21 (2023).
38. Jenson, J. M., Li, T., Du, F., Ea, C.-K. & Chen, Z. J. Ubiquitin-like conjugation by bacterial cGAS enhances anti-phage defence. *Nature* **616**, 326–331 (2023).
39. Spear, A. M., Loman, N. J., Atkins, H. S. & Pallen, M. J. Microbial TIR domains: not necessarily agents of subversion? *Trends Microbiol.* **17**, 393–398 (2009).
40. Gerdts, J., Brace, E. J., Sasaki, Y., DiAntonio, A. & Milbrandt, J. SARM1 activation triggers axon degeneration locally via NAD^+ destruction. *Science* **348**, 453–457 (2015).
41. Essuman, K. et al. The SARM1 Toll/Interleukin-1 receptor domain possesses intrinsic NAD^+ cleavage activity that promotes pathological axonal degeneration. *Neuron* **93**, 1334–1343.e5 (2017).
42. Horsefield, S. et al. NAD^+ cleavage activity by animal and plant TIR domains in cell death pathways. *Science* **365**, 793–799 (2019).
43. Huang, S. et al. Identification and receptor mechanism of TIR-catalyzed small molecules in plant immunity. *Science* **377**, eabq3297 (2022).
44. Rousset, F. et al. TIR signaling activates caspase-like immunity in bacteria. *Science* **387**, 510–516 (2025).

Publisher's note Springer Nature remains neutral with regard to jurisdictional claims in published maps and institutional affiliations.

Springer Nature or its licensor (e.g. a society or other partner) holds exclusive rights to this article under a publishing agreement with the author(s) or other rightsholder(s); author self-archiving of the accepted manuscript version of this article is solely governed by the terms of such publishing agreement and applicable law.

© The Author(s), under exclusive licence to Springer Nature Limited 2025

Methods

Bacteria growth conditions

For the experiments presented in Figs. 1 and 2 and Extended Data Figs. 1, 3 and 4, *B. subtillis* were grown in MMB (LB supplemented with 0.1 mM $MnCl_2$ and 5 mM $MgCl_2$) in a liquid medium with shaking at 200 rpm at 37 °C or 25 °C as stated in Supplementary Table 1, or on LB 1.5% agar plates. The antibiotics spectinomycin (100 μg ml^{-1}) or chloramphenicol (5 μg ml^{-1}) were used to ensure the presence of an integrated antibiotics resistance cassette in the *B. subtilis* BEST7003 genomic *amyE* or *thrC* locus, respectively. When applicable, 1 mM or 0.1 mM IPTG was added to bacterial cultures to induce gene expression as stated in Supplementary Table 1. A list of all bacterial strains and phages used in this study can be found in Supplementary Table 1.

Cloning and transformation

The shuttle vectors used in this study, as well as the DNA for the Thoeris genes or Thoeris anti-defence genes were constructed in previous studies[6,9]. Thoeris defence systems or Thoeris ThsA genes were cloned under native promoters in the shuttle vector pSG1-rfp[6] that contains the spectinomycin-resistance gene, and the cloned sequence with the spectinomycin-resistance gene was integrated into the *B. subtilis amyE* locus. As a negative control, a transformant with an empty insert containing only the spectinomycin-resistance gene in the *amyE* locus was used.

Anti-Thoeris genes or Thoeris ThsB genes were cloned under an IPTG inducible promoter (Phspank) in the shuttle vector pSG-thrC-phSpank[9] that contains the chloramphenicol-resistance gene, and the cloned vector was integrated into *B. subtilis thrC* locus in the appropriate background (Supplementary Table 1). As a negative control, a transformant with an identical plasmid, containing GFP instead of an anti-Thoeris gene or a *thsB* gene, was used and integrated into the *thrC* locus.

To generate the plasmids used in this study, genes were amplified using KAPA HiFi HotStart ReadyMix (Roche, KK2601), cloned using NEBuilder HiFi DNA Assembly cloning kit (NEB, E5520S) and transformed to NEB 5-alpha Competent *E. coli* High Efficiency (NEB). For one-fragment DNA assembly, the linear plasmid obtained by PCR was ligated using the KLD enzyme mix (NEB, M0554S) according to the manufacturer's protocol before transformation. For assembly of more than one fragment, PCR products were treated with the FastDigest DpnI (ThermoFisher) restriction enzyme according to the manufacturer's protocol. The fragments were then assembled using the NEBuilder HiFi DNA Assembly Master Mix before transformation. Plasmids purified from an overnight culture were then transformed into *B. subtilis* BEST7003. Transformation was performed using MC medium as previously described[6].

For mutagenesis, plasmids were amplified using Phusion High-Fidelity DNA Polymerase (Thermo Fisher, F530L) phosphorylated with T4 Polynucleotide Kinase (Thermo Fisher, EK0032) and ligated with T4 DNA ligase (Thermo Fisher, EL0011). A list of all plasmids and primers used in this study can be found in Supplementary Table 2.

SBSphiJ propagation

Overnight liquid cultures of *B. subtilis* cells were diluted 1:100 in 100 ml MMB and grown at 25 °C, 200 rpm shaking to an OD_{600} of 0.3. At this stage, phage SBSphiJ was added to the liquid culture at an MOI of 0.1 and incubation at 25 °C, 200 rpm shaking continued until culture collapse. The culture was then centrifuged at 4 °C for 10 min at 3,200*g*, and the supernatant was filtered through a 0.22-μm filter to eliminate remaining bacteria and large debris.

Plaque assays

Phage SBSphiJ titre was determined using the small drop plaque assay method[45]. 400 μl of an overnight culture of bacteria grown in MMB with antibiotics were mixed with 30 ml pre-melted 0.5 % MMB agar and poured into a 10 cm square plate. For induction of genes expressed under the Phspank promoter, IPTG was added to a final concentration of 1 mM or 0.1 mM before plating (Supplementary Table 1). After incubation for 1 h at room temperature, 10 μl drops from 10-fold serial dilutions of the phage lysate in MMB were dropped on top of the bacterial layer. After the drops dried up, plates were incubated at 25 °C overnight. PFUs were determined by counting the derived plaques, and lysate titre was determined by calculating PFU per ml. When no individual plaques could be identified, a faint lysis zone across the drop area was considered to be 10 plaques. Bacterial defence phenotype was measured as the ratio between the PFU per ml on control bacteria and PFU per ml on bacteria expressing a Thoeris system.

Phage infection dynamics in liquid medium

Overnight cultures of *B. subtilis* cells expressing a Thoeris system or an empty insertion were diluted 1:100 in MMB medium supplemented with spectinomycin (100 μg ml^{-1}). Cultures were incubated at 25 °C with shaking 200 rpm until cells reached OD_{600} of 0.3. At this point, 180 μl of the culture was transferred into a 96-well plate containing additional 20 μl of MMB for the uninfected control or phage SBSphiJ for a final MOI of 0.1 or 10. Plates were incubated at 25 °C with shaking in a TECAN Infinite M200 plate reader, and OD_{600} was measured every 4 min.

NADase activity assay with purified *Bc*ThsA

Lysates for this assay were prepared from an overnight culture of *B. subtilis* cells expressing $ThsB_{cereus}$, *Ba*ThsB, or control cells expressing GFP. Cells were diluted 1:100 in 100 ml MMB medium supplemented with 1 mM IPTG and chloramphenicol (5 μg ml^{-1}), and grown at 25 °C, 200 rpm shaking until reaching an OD_{600} of 0.3. At this point, SBSphiJ phage was added at an MOI of 10, and cultures were incubated at 25 °C for 120 min. Then, 50 ml samples were collected and centrifuged at 4 °C, 3,200*g* for 10 min to pellet the cells. The supernatant was discarded, and the pellet was flash-frozen and stored at −80 °C.

To extract the cell metabolites from frozen pellets, 600 μl of 0.1 M sodium phosphate buffer, pH 8.0, was added to each pellet and incubated at room temperature for 10 min, and then transferred to ice. Then, the samples were transferred to a FastPrep Lysing Matrix B in a 2 ml tube (MP Biomedicals, 116911100) and lysed at 4 °C using a FastPrep bead beater for 2× 40 s at 6 m s^{-1}. Tubes were then centrifuged at 4 °C for 10 min at 15,000*g*. Supernatant was transferred to Amicon Ultra-0.5 Centrifugal Filter Unit 3 kDa (Merck Millipore, UFC500396) and centrifuged for 45 min at 4 °C, 12,000*g*. Filtered cell lysates were taken for in vitro *Bc*ThsA activity assay.

*Bc*ThsA was expressed and purified as described in a previous study[15]. The NADase reaction was performed in black 96-well half-area plates (Corning, 3694). In each reaction well, purified 2 μl *Bc*ThsA protein was added to 43 μl filtered cell lysates (final concentration 100 nM). Five microlitres of 5 mM nicotinamide 1,N^6-ethenoadenine dinucleotide (εNAD$^+$, Sigma, N2630) was added to each well immediately before measurements. Plates were incubated inside a Tecan Infinite M200 plate reader at 25 °C, and measurements were taken at 300 nm excitation wavelength and 410 nm emission wavelength every 15 s. Reaction rate was calculated from the linear part of the initial reaction.

Preparation of filtered cell lysates for LC–MS analysis

For generating filtered cell lysates that contain TIR-catalysed signalling molecules, we used *B. subtilis* cells expressing *Ba*ThsB or GFP for control under an inducible Phpsank promoter. These cultures were grown overnight and then diluted 1:100 in 250 ml MMB medium supplemented with 1 mM IPTG and chloramphenicol (5 μg ml^{-1}) and grown at 37 °C, 200 rpm shaking for 90 min, followed by additional incubation and shaking at 25 °C, 200 rpm until reaching an OD_{600} of 0.3. At this point, SBSphiJ phages were added at an MOI of 10, and cultures were incubated at 25 °C for 120 min. Then, 200 ml samples were collected and centrifuged at 4 °C, 3,200*g* for 10 min to pellet the cells.

The supernatant was discarded, and the pellet was flash-frozen and stored at −80 °C. Cell metabolites were extracted as mentioned above for *Bc*ThsA activity assay, and filtered cell lysates were sent for liquid chromatography–mass spectrometry (LC–MS) analysis.

Isolation of type II *Ba* Thoeris signalling molecule for LC–MS analysis

To isolate the *Ba*ThsB signalling molecule, 100 µl of filtered cell lysates derived from cells expressing *Ba*ThsB or GFP were incubated at room temperature for 1 h with 75 µl 0.1 M sodium phosphate buffer, pH 8 and 25 µl purified *Mo*Tad2 protein (67 µM, 0.66 mg ml^{-1}) to capture the molecule. Following incubation, the mixture was transferred to Amicon Ultra-0.5 Centrifugal Filter Unit 3 kDa and centrifuged for 20 min at 4 °C, 12,000*g*. This filtrate was sent to LC–MS analysis. To remove the metabolites that did not bind *Mo*Tad2, the columns were washed 4 times by adding 400 µl 0.1 M sodium phosphate buffer, pH 8, and centrifuged for 20 min at 4 °C, 12,000*g*. *Mo*Tad2 was recovered by flipping the 3 kDa filter, transferring it to a new tube, and centrifuging it for 5 min at 4 °C, 1,000*g*. To collect the *Mo*Tad2-bound molecules, *Mo*Tad2 was denatured for 25 min at 98 °C. To remove the *Mo*Tad2 protein, the sample was filtered in an Amicon Ultra-0.5 Centrifugal Filter Unit 10 kDa (Merck Millipore, UFC501096) supplemented with a 100 µl of 0.1 M sodium phosphate buffer, pH 8, and centrifuged 20 min at 4 °C, 12,000*g*. The purified molecules were sent to LC–MS analysis.

LC–MS analysis

Prior to the LC–MS analysis, samples were centrifuged twice at 18,000*g* to remove possible precipitants and transferred to a HPLC vial. For experiments presented in Fig. 2d,e and Extended Data Figs. 3a,b and 4a,b, samples were analysed as described previously[46], with minor modifications described below. In brief, analysis was performed using Acquity I class UPLC System combined with mass spectrometer Q Exactive Plus Orbitrap (Thermo Fisher Scientific), which was operated in positive and negative ionization modes. The mass spectra were acquired with 70.000 resolution, scan range of 400–2,000 *m*/*z*. For the identification of the compounds, we used a data-dependent acquisition, top 5 method. The LC separation was done using the SeQuant ZIC-pHILIC (150 mm × 2.1 mm) with the SeQuant guard column (20 mm × 2.1 mm) (Merck). The mobile phase B was acetonitrile, and the mobile phase A was 20 mM ammonium carbonate with 0.1% ammonia hydroxide in an 80:20 solution (v/v) of double-distilled water and acetonitrile. The flow rate was kept at 200 µl min^{-1}, and the gradient was as follows: 75% of B (0–2 min), decreased to 25% of B (2–14 min), 25% of B (14–18 min), increased to 75% of B (18–19 min), 75% of B (19–23 min). The data was analysed using MZmine 2.5.3 software.

Untargeted mass spectrometry data from all samples were integrated, and the signalling molecule generated by *Ba*ThsB was identified by searching for molecules enriched in *Ba*ThsB filtered cells lysates prior to *Mo*Tad2 incubation and post *Mo*Tad2 denaturation but absent in *Ba*ThsB filtered cell lysates post *Mo*Tad2 incubation and control cells that lack *Ba*ThsB. The analysis was performed for the mass spectrometry measurements derived from both positive and negative ionization modes. To define the *m*/*z* value and retention time of His-ADPR, the same analysis as before was repeated on the mass spectrometry results of *Ba*ThsB filtered cells lysates, with the exception that the parameters in the MZmine 'Chromatogram deconvolution' feature were adjusted to engulf the same peak in two repeats.

For experiments presented in Extended Data Figs. 5a and 6a,b, LC–MS analysis was carried out on 1290 Infinity HPLC system (Agilent Technologies) coupled to a 6520 Accurate Mass Q-TOF LC–MS mass analyser (Agilent Technologies) with an electrospray ion source. HPLC was carried out on a Supelco Discovery HS C18 column at a temperature of 30 °C. Chromatography was performed at a 0.3 ml min^{-1} flow rate using a linear mobile phase gradient over 30 min, from 0.02% formic acid in water to 0.02% formic acid in acetonitrile. Mass spectrometry was carried out using gas at 300 °C, 10 l min^{-1} gas flow, 2,500 V capillary voltage, 150 V fragmentator voltage. Data acquisition and analysis were done using QTOF Acquisition Software (B.02.01 SP1) and MassHunter (vB.05.00, Agilent Technologies) software.

Protein expression and purification

_Mo_Tad2 protein expression and purification for biochemistry. Expression of *Mo*Tad2 was performed using the expression vector pET28-bdSumo. This vector was constructed by transferring the His14-bdSUMO cassette from the expression vector (Designated K151) provided by D. Görlich[47] into the expression vector pET28-TevH[48]. Cloning was performed by the restriction-free method[49]. A 5 l culture of BL21(DE3) harbouring the vector was induced with 200 µM IPTG and grown at 15 °C overnight. The cells were collected and lysed by a cell disrupter (Constant Systems) in a buffer comprising 50 mM Tris pH 8, 0.5 M NaCl, 30 mM imidazole, 1 mM $MgCl_2$, and containing 200 KU/100 ml lysozyme, 20 µg ml^{-1} DNase, 1 mM phenylmethylsulfonyl fluoride (PMSF) and protease inhibitor cocktail. After clarification of the supernatant by centrifugation, the lysate was incubated with 5 ml pre-washed Ni^{2+} beads (Adar Biotech) for 1 h at 4 °C. After removing the supernatant, the beads were washed four times with PBS buffer. The cleaved protein (without tags) was eluted from the beads by incubation of the beads with 5 ml cleavage buffer: PBS supplemented with 250 mM sucrose and 10% glycerol containing 0.1 mg bdSumo protease (without His tag) for 2 h at room temperature. The supernatant containing the cleaved protein was removed and applied to a size-exclusion column (HiLoad 16/60 Superdex 75 prep-grade, GE Healthcare) equilibrated with PBS. The pure protein was pooled and frozen in aliquots stored at −80 °C.

Expression and purification of _Mo_Tad2 for crystallization. *Mo*Tad2 was codon-optimized (GeneArt), synthesized as DNA fragments (Integrated DNA Technologies), and cloned by Gibson assembly into a custom pET vector with an N-terminal 6× His-SUMO tag and an ampicillin resistance gene. The plasmid was transformed into BL21(DE3) RIL *E. coli* (Agilent), colonies were grown on 1.5% agar MDG plates (2 mM $MgSO_4$, 0.5% glucose, 25 mM Na_2HPO_4, 25 mM KH_2PO_4, 50 mM NH_4Cl, 5 mM Na_2SO_4, 0.25% aspartic acid and 2–50 µM trace metals, 100 µg ml^{-1} ampicillin and 34 µg ml^{-1} chloramphenicol), and 3 colonies were picked to inoculate separate 30 ml MDG starter cultures, which were grown overnight at 37 °C. One litre of M9ZB expression culture (2 mM $MgSO_4$, 0.5% glycerol, 47.8 mM Na_2HPO_4, 22 mM KH_2PO_4, 18.7 mM NH_4Cl, 85.6 mM NaCl, 1% Cas-amino acids, 2–50 µM trace metals, 100 µg ml^{-1} ampicillin, and 34 µg ml^{-1} chloramphenicol) was seeded with 15 ml MDG starter culture, grown to OD_{600} of 2.5 at 37 °C with, and induced with 0.5 mM IPTG and lowering of temperature to 16 °C. After 16–20 h, 2 l of culture was collected by centrifugation, resuspended in 120 ml of lysis buffer (20 mM HEPES-KOH pH 7.5, 400 mM NaCl, 30 mM imidazole, 10% glycerol, and 1 mM DTT), lysed by sonication, and clarified by centrifugation. Supml ernatant was passed over 8 ml of Ni-NTA resin (Qiagen), and the resin was washed with 70 ml of lysis buffer supplemented with 1 M NaCl, followed by 20 ml lysis buffer. Protein was eluted with 20 ml of lysis buffer supplemented with 300 mM imidazole and dialysed overnight at 4 °C using 14 kDa dialysis tubing in size-exclusion buffer (20 mM HEPES-KOH pH 7.5, 250 mM KCl and 1 mM TCEP) in the presence of recombinant human-SENP2 to induce SUMO-tag cleavage. Protein was further purified by size-exclusion chromatography on a Superdex 75 16/600 column (Cytiva). Peak fractions were collected, concentrated to >50 mg ml^{-1}, flash-frozen in liquid nitrogen, and stored at −80 °C. Crystallographic experiments revealed that HEPES competed for binding with His-ADPR. The buffer system was subsequently replaced with Tris-HCl pH 7.5 for *Mo*Tad2 purification and co-crystallization with His-ADPR.

Expression and purification of _Ba_Macro for crystallization and His-ADPR purification. Expression of *Ba*Macro (*Ba*ThsA residues

83–297, with C-terminal TwinStrep tag) was performed using the expression vector pBAD-DelTM-ThsA-TwinStrep_*Ba*ThsB-His, which was generated from the type II Thoeris amylo operon by removing the TM domain of *Ba*ThsA (residues 1–82) and genetically fusing a C-terminal TwinStrep tag. In addition, a C-terminal His_6 tag was fused to the C terminus of ThsB. The coding sequence of the operon was codon-optimized for *E. coli* and synthesized by TWIST Biosciences. The operon was then cloned into the NcoI/HindIII site of a pBAD-His backbone by Twist Bioscience. A 5 l culture of *E. coli* TOP10 cells harbouring the vector was induced with 0.2% L-arabinose and grown overnight at 16 °C. The cells were collected by centrifugation and resuspended in the purification buffer (20 mM Tris-HCl (pH 8.0 at 25 °C), 1 M NaCl, 5 mM 2-mercaptoethanol, 0.1% Triton X-100) supplemented with 2 mM PMSF and 5% (v/v) glycerol and lysed by sonication. After removing cell debris by centrifugation, the supernatant was loaded on Strep-Tactin XT Superflow column (IBA), and the bound protein was eluted with 50 mM D-biotin solution in the purification buffer. Fractions with the protein of interest were pooled, concentrated up to 5 ml using Amicon Ultra-15 centrifugal filter unit (Merck Millipore) and loaded on a HiLoad 16/600 Superdex 200 gel filtration column (Cytiva) equilibrated with the purification buffer containing 0.01% Triton X-100. Peak fractions containing the protein of interest were pooled. Purified protein was dialysed against 20 mM Tris-HCl (pH 8.0 at 25 °C), 500 mM NaCl, 2 mM DTT, 0.01% Triton X-100, and 50% (v/v) glycerol buffer and stored at −20 °C. The final protein concentrations were determined by measuring absorbance at 280 nm using sequence-predicted extinction coefficients.

Expression and purification of *Ba*Macro and ThsB proteins for biochemical analysis. The cells containing TwinStrep–*Ba*Macro (wild type and mutants), *E. rectale* ThsB–TwinStrep and *Ba*ThsB–TwinStrep were collected by centrifugation and resuspended in the purification buffer (20 mM Tris-HCl (pH 8.0 at 25 °C), 500 mM NaCl, 5 mM 2-mercaptoethanol) supplemented with 2 mM PMSF and 5% (v/v) glycerol and lysed by sonication. After removing cell debris by centrifugation, the supernatants with TwinStrep–*Ba*Macro, *Er*ThsB–TwinStrep or *Ba*ThsB–TwinStrep proteins were loaded on Streptrap XT column (Cytiva), and the bound protein was eluted with 50 mM D-biotin solution in the purification buffer. Fractions with all the proteins of interest were pooled, concentrated, and loaded on a Superdex 200 gel filtration column (Cytiva) equilibrated with the purification buffer. Peak fractions containing the protein of interest were pooled. Purified protein was dialysed against 20 mM Tris-HCl (pH 8.0 at 25 °C), 500 mM NaCl, 2 mM DTT, and 50% (v/v) glycerol buffer and stored at −20 °C. The final protein concentrations were determined by measuring absorbance at 280 nm using sequence-predicted extinction coefficients.

Purification of His-ADPR

Purified C-terminal tagged *Ba*Macro domain was concentrated up to 1 ml using Amicon Ultra-4 centrifugal filter unit (Merck Millipore). Retentate was then subjected to heat denaturation at 98 °C for 5 min with agitation. The resulting mixture was centrifuged at 18,000*g* for 15 min, and the resulting supernatant was subjected to HPLC purification. Agilent 1100 HPLC system equipped with Agilent Prep-C18 reversed-phase HPLC column (Agilent, 443905-102) was used for HPLC. For mobile phase A 20 mM ammonium formate (pH 6.9 at 25 °C) was used, and for mobile phase B 100% methanol was used. A 5 min isocratic mode of mobile phase A followed by 5% mobile phase B gradient over 10 min was used at a flow rate of 17 ml min^{-1}. Collected fractions were checked by LC–MS analysis.

His-ADPR synthesis in vitro

To produce the signalling molecule in vitro, reactions containing 1 mM NAD^+, 3 mM L-histidine, 1 μM apo *Ba*Macro, and 100 μM ThsB were prepared in reaction buffer containing 10 mM Na-HEPES (pH 7.5 at 25 °C), 150 mM NaCl and 5 mM $MgCl_2$ and incubated for 1 day at 25 °C and later 6 days at 37 °C. Samples were heat-denatured for 5 min at 98 °C, centrifuged for 15 min at 16,000*g*, and the resulting supernatant was analysed by LC–MS.

E. coli survivability spot assay

E. coli cells, transformed with pBAD-TwinStrep-ThsA or pBAD-GFP plasmids, were grown overnight at 37 °C in liquid LB supplemented with carbenicillin (50 μg ml^{-1}). The overnight culture was inoculated in a 1:100 ratio into fresh MMB supplemented with carbenicillin (50 μg ml^{-1}), grown until OD_{600} reached 0.05 and L-arabinose was added to a final concentration of 0.2%. After the induced *E. coli* cells reached OD_{600} of around 0.6, the cultures were normalized to an OD_{600} of 0.3 using MMB media supplemented with 0.2% L-arabinose and carbenicillin (50 μg ml^{-1}). Normalized culture was aliquoted in 8 μl into sterile PCR tubes, and 2 μl of His-ADPR in different concentrations or ultrapure water was added. Cells were incubated at 37 °C with 300 rpm shaking for 1 h, then serially diluted in fresh MMB media and plated onto LB media agar plates supplemented with carbenicillin (50 μg ml^{-1}). Bacteria were grown at 37 °C for 16 h. The experiment was performed in triplicate.

Dynamic light scattering

A 10 μl sample was prepared by mixing *Ba*Macro domain or mutant with His-ADPR or buffer control to a final concentration of 5 or 10 μM protein and specified concentration of His-ADPR. The sample was loaded into a 2 μl Quartz Cuvette (Malvern Panalytical), and measurements were carried out at 25 °C with a Zetasizer μV photometer (Malvern Panalytical) using Zetasizer Software (v6.20). Measurements were carried out in 60 s runs containing 6× 10 s runs with 10 measurements in total.

Thermal shift assay

The sample was prepared by mixing *Ba*Macro domain (wild type or mutant) with His-ADPR or buffer control to a final concentration of 5 μM protein and 50 μM His-ADPR. The sample was loaded into capillaries, and 330 nm and 350 nm fluorescence and light scattering were measured in Prometheus NT.48 (NanoTemper) during incubation in temperatures rising at the speed of 0.5 °C min^{-1}. The data were processed using PR. Therm Control (v2.3.1) software. The resulting melting temperatures from $n = 3$ technical replicates for the corresponding apo and His-ADPR-bound samples were averaged and subtracted to calculate the change in melting temperature ΔT_m. Standard deviation of this value (difference s.d.) was calculated by taking a square root of the sum of sample variances.

Western blot analysis of mutant *Ba*ThsA expression

E. coli cells, transformed with pBAD-TwinStrep-ThsA and mutant plasmids, were grown overnight at 37 °C in liquid LB supplemented with carbenicillin (50 μg ml^{-1}). The overnight culture was inoculated in a 1:100 ratio into fresh LB supplemented with carbenicillin (50 μg ml^{-1}), grown until OD_{600} reached ~0.6, and L-arabinose was added to a final concentration of 0.2%. Induced cells were grown overnight at 16 °C. Collected cells were washed, their amounts normalized, and cells were resuspended in lysis buffer (20 mM HEPES (pH 7.5 at 25 °C), 150 mM NaCl, 2 mM PMSF, 2 mg ml^{-1} lysozyme, 10 U ml^{-1} benzonase). The mixture was slowly agitated for 2 h at 4 °C. Then, SDS was added to a final concentration of 2%, and the cells were further agitated for 30 min at 4 °C. The resulting mixture was centrifuged, and the resulting supernatant was used in SDS–PAGE followed by western blot analysis using Strep-Tactin AP conjugate (IBA, 2-1503-001) following the manufacturer's protocol. Two replicates were performed (Supplementary Fig. 1).

Size-exclusion chromatography with multi-angle light scattering

Size-exclusion chromatography with multi-angle light scattering of *Ba*Macro domain (wild type and mutants) was carried out at room temperature using a Superdex 200 Increase 10/300 GL column (Cytiva) pre-equilibrated with buffer (10 mM Na-HEPES (pH 7.0 at 25 °C), 150 mM

NaCl), at 0.4 ml min^{-1} flow rate. A 200 µl sample of 5 µM protein was loaded onto the column. The light scattering signals were monitored on a miniDawn TREOS II detector; concentrations of protein samples were measured using an Optilab T-rEX refractive index detector (Wyatt Technologies). Data were analysed in Astra software (Wyatt Technologies) using a d*n*/d*c* value of 0.185 ml g^{-1}.

Crystallization and structure determination of *Ba*Macro

Crystallization and structure determination of the *Ba*Macro domain. *Ba*Macro domain initial needle-shaped crystals were obtained by the sitting-drop vapour diffusion method from 6.9 mg ml^{-1} protein solution in the concentration buffer (20 mM Tris-HCl (pH 8.0 at 25 °C), 250 mM NaCl, 2 mM DTT, 0.01 % Triton X-100) mixed in 7:3 ratio with reservoir solution (25% (w/v) polypropylene glycol (PEG) 10,000, 0.1 M Tris-acetate (pH 8.0 at 25 °C), 0.1 M KCl, 0.05 M magnesium formate) at 20 °C. The needle-shaped crystals were used for microseeding. Crystals, used for a structure determination, were obtained by the sitting-drop vapour diffusion method from 5 mg ml^{-1} protein solution in the concentration buffer, reservoir solution (23.75% PEG 3500, 0.1 M Bis-Tris (pH 6.5 at 25 °C), 0.19 M ammonium sulfate, 5% (v/v) glycerol) and seeding solution mixed in a 4:3:1 ratio.

The X-ray diffraction dataset was collected to the nominal resolution of 2.23 Å at the EMBL/DESY Petra III P13 beamline (Hamburg, Germany) at 100 K, wavelength 0.9800 Å. XDS (version 15 March 2019)[50], SCALA and TRUNCATE (CCP4 package 7.0.076)[51] were used for data processing. The structure was solved by molecular replacement by Phaser[52] using an ensemble of 5 models obtained from Robetta server[53] and rebuilt by Phenix AutoBuild[54]. The model was improved by several cycles of refinement in Phenix (phenix-1.20.1-4487)[55] and manual inspection in Coot 0.9.7[56]. Cif file for His-ADPR refinement was prepared using eLBOW[57], bond lengths were corrected using data from ref. 58 and His.cif from Coot. C-terminal residues of the domain are disordered; the final model contains residues 83–293 in chain A and 83–289 in chain B. 96.38 % of the residues are in the favoured and 3.62 % in the allowed region of the Ramachandran plot. The data collection and refinement statistics are presented in Extended Data Table 1. The molecular graphics figures were prepared with PyMOL (v.2.3.0) (The PyMOL Molecular Graphics System).

*Mo*Tad2 crystallization and structural analysis

Crystals of *Mo*Tad2 were grown by the hanging-drop vapour diffusion method using EasyXtal 15 well trays (NeXtal). First, protein was prepared at 10 mg ml^{-1} in crystallization buffer (20 mM HEPES-KOH pH 7.5, 80 mM KCl and 1 mM TCEP). Two-microlitre hanging drops of 1 µl protein and 1 µl reservoir solution were set above 400 µl of reservoir solution (0.1 M $MgCl_2$, 0.1 M sodium acetate pH 4.6, 25% (w/v) PEG 400). Crystals were grown for 1 week before collection by flash freezing in liquid nitrogen. X-ray diffraction data were collected at the Advanced Photon Source (beamlines 24-ID-C and 24-ID-E) with RAPD, and data were processed using the SSRL autoxds script (A. Gonzalez). Phases were determined by molecular replacement using a truncated predicted structure of *Mo*Tad2 (apo) from ColabFold v1.5.3[59]. Model building was performed in Coot 0.8.9.3[56], with refinement in Phenix 1.21.1[60]. Final structures were refined to stereochemistry statistics for Ramachandran plot (favoured/allowed), rotamer outliers, and MolProbity score as follows: *Mo*Tad2 apo, 98.7%/1.3%, 3.4%, 1.74. A summary of crystallographic statistics is provided in Extended Data Table 1.

*Mo*Tad2–His-ADPR complex crystallization and structural analysis. *Mo*Tad2–His-ADPR complex was grown using the hanging-drop vapour diffusion method at 18 °C. Recombinant *Mo*Tad2 was diluted to 2 mg ml^{-1} in a buffer containing 20 mM Tris-HCl pH 7.5, 100 mM KCl, and 1 mM TCEP. The diluted protein was incubated with 200 µM His-ADPR on ice for 10 min and allowed to equilibrate to 18 °C for 1 h. Following equilibration, crystals were grown in 96-well trays by mixing 200 nl of the protein mixture and 200 nl of reservoir solution (0.1 M CH_3COONa pH 4.4 and 24% PEG4000). Crystals were cryoprotected with reservoir solution supplemented with 16% ethylene glycol and 100 µM His-ADPR and collected by flash freezing in liquid nitrogen. X-ray diffraction data were collected at the National Synchrotron Light Source II (NSLS2) beamline 17-ID-2 (FMX) with blueskey v1.6.7. Data were processed with autoPROC 10.07.2024[61] and Aimless 0.7.9[62]. Experimental phase information was determined by molecular replacement using Phaser-MR in Phenix 1.21.1[60] using a model of apo *Mo*Tad2. Model building was performed using Coot 0.8.9.3[56] and refined using PHENIX. A summary of crystallographic statistics is provided in Extended Data Table 1. Structural figures were generated using PyMOL (version 2.5.4).

Reporting summary

Further information on research design is available in the Nature Portfolio Reporting Summary linked to this article.

Data availability

All data are available in the Article and the supplementary material. Strains of bacteria and phages and plasmid maps of the constructs used for the experiments are attached as Supplementary Tables 1 and 2. The atomic coordinates and structure factors have been deposited in the Protein Data Bank (PDB) under accession codes 8V3E (*Mo*Tad2), 9EIB (His-ADPR-bound *Mo*Tad2) and 8R66 (His-ADPR-bound *Ba*Macro).

45. Mazzocco, A., Waddell, T. E., Lingohr, E. & Johnson, R. P. in *Methods in Molecular Biology*, vol. 501 (eds Clokie, M. R. & Kropinski, A. M.) 81–85 (Humana Press, 2009).
46. Zheng, L. et al. Fumarate induces redox-dependent senescence by modifying glutathione metabolism. *Nat. Commun.* **6**, 6001–6001 (2015).
47. Frey, S. & Görlich, D. A new set of highly efficient, tag-cleaving proteases for purifying recombinant proteins. *J. Chromatogr. A* **1337**, 95–105 (2014).
48. Peleg, Y. & Unger, T. in *Methods in Molecular Biology*, vol. 426 (eds Kobe, B., Guss, M. & Huber, T.) 197–208 (Humana Press, 2008).
49. Unger, T., Jacobovitch, Y., Dantes, A., Bernheim, R. & Peleg, Y. Applications of the restriction free (RF) cloning procedure for molecular manipulations and protein expression. *J. Struct. Biol.* **172**, 34–44 (2010).
50. Kabsch, W. XDS. *Acta Crystallogr. D* **66**, 125–132 (2010).
51. Collaborative Computational Project, No. 4. The CCP4 suite: programs for protein crystallography. *Acta Crystallogr. D* **50**, 760–763 (1994).
52. McCoy, A. J. et al. Phaser crystallographic software. *J. Appl. Crystallogr.* **40**, 658–674 (2007).
53. Song, Y. et al. High-resolution comparative modeling with RosettaCM. *Structure* **21**, 1735–1742 (2013).
54. Terwilliger, T. C. et al. Iterative model building, structure refinement and density modification with the PHENIX AutoBuild wizard. *Acta Crystallogr. D* **64**, 61–69 (2008).
55. Afonine, P. V. et al. Towards automated crystallographic structure refinement with phenix.refine. *Acta Crystallogr. D* **68**, 352–367 (2012).
56. Emsley, P. & Cowtan, K. Coot: model-building tools for molecular graphics. *Acta Crystallogr. D* **60**, 2126–2132 (2004).
57. Moriarty, N. W., Grosse-Kunstleve, R. W. & Adams, P. D. Electronic Ligand Builder and Optimization Workbench (eLBOW): a tool for ligand coordinate and restraint generation. *Acta Crystallogr. D* **65**, 1074–1080 (2009).
58. Heyrovska, R. Structures of the molecular components in DNA and RNA with bond lengths interpreted as sums of atomic covalent radii. *Open Struct. Biol. J.* **2**, 1–7 (2008).
59. Mirdita, M. et al. ColabFold: making protein folding accessible to all. *Nat. Methods* **19**, 679–682 (2022).
60. Liebschner, D. et al. Macromolecular structure determination using X-rays, neutrons and electrons: recent developments in Phenix. *Acta Crystallogr. D* **75**, 861–877 (2019).
61. Vonrhein, C. et al. Data processing and analysis with the autoPROC toolbox. *Acta Crystallogr. D* **67**, 293–302 (2011).
62. Evans, P. R. & Murshudov, G. N. How good are my data and what is the resolution? *Acta Crystallogr. D* **69**, 1204–1214 (2013).

Acknowledgements The authors thank O. Izsak for help with mass spectrometry analysis; M. Itkin and S. Malitsky for conducting the mass spectrometry experiments; Y. Peleg and S. Albeck for assistance with *Mo*Tad2 purification; M. Malikenas for assisting in His-ADPR purification procedure; and Sorek laboratory members for comments on earlier versions of this manuscript. X-ray diffraction data were collected at the beamline P13 operated by EMBL Hamburg at the PETRA III storage ring (DESY, Hamburg, Germany) and at the Northeastern Collaborative Access Team beamlines 24-ID-C and 24-ID-E (P30 GM124165). Access to the EMBL P13 beamline has been supported by iNEXT-Discovery, project number 871037, funded by the Horizon 2020 programme of the European Commission. NE-CAT data collection was supported by use of a Pilatus detector (S10RR029205), an Eiger detector (S10OD021527), and the Argonne National Laboratory Advanced Photon Source (DE-AC02-06CH11357). R.S. was supported, in part, by the European Research Council (grant ERC-AdG GA 101018520), Israel Science Foundation (MAPATS grant 2720/22), the Deutsche Forschungsgemeinschaft

(SPP 2330, grant 464312965), the Ernest and Bonnie Beutler Research Program of Excellence in Genomic Medicine, Dr. Barry Sherman Institute for Medicinal Chemistry, Miel de Botton, the Andre Deloro Prize, and the Knell Family Center for Microbiology. P.J.K. was supported, in part, by the Pew Biomedical Scholars programme and The G. Harold and Leila Y. Mathers Charitable Foundation. G.T. was supported by the Research Council of Lithuania (LMTLT) agreement no. S-MIP-21-6. E.H. was supported by the Israel Cancer Research Fund Postdoctoral Fellowship. E.Y. was supported by the Clore Scholars Program, and, in part, by the Israeli Council for Higher Education (CHE) via the Weizmann Data Science Research Center.

Author contributions M.Z., D.S., C.A., P.J.K., R.S. and G.T. designed the research. C.A. carried out bacterial genetic and phage infection assays, phage infection dynamics, His-ADPR pulldown from lysates, biochemical experiments and mass spectrometry analyses. I.O., G.A. and E.H. carried out biochemical experiments and mass spectrometry analyses. E.Y. carried out a phylogenetic analysis of Tad2. A. Leavitt carried out bacterial genetics and phage infection assays. D.S. and D.V. performed cloning and mutagenesis of ThsA and its *Ba*Macro domain. A.S. carried out the type II Thoeris proteins purifications. D.S. and M.Z. characterized *Ba*Macro and its mutants, performed *E. coli* survivability assay, western blot analysis and biochemical experiments and analysed the results. A.R. carried out mass spectrometry analysis. D.S. crystallized *Ba*Macro–His-ADPR complex and D.S. and G.T. solved its structure. D.S. and A.S purified His-ADPR. A. Lu crystallized apo *Mo*Tad2 and solved its structure. R.B.C. crystallized *Mo*Tad2–His-ADPR complex and solved its structure with assistance from H.C.T. D.S., C.A., P.J.K., R.S. and G.T. wrote the manuscript with input from all authors. All authors reviewed and edited the manuscript and supported the conclusions.

Competing interests R.S. is a scientific cofounder and advisor of BiomX and Ecophage. The other authors declare no competing interests.

Additional information

Supplementary information The online version contains supplementary material available at https://doi.org/10.1038/s41586-025-08930-2.

Correspondence and requests for materials should be addressed to Philip J. Kranzusch, Rotem Sorek or Giedre Tamulaitiene.

Peer review information *Nature* thanks the anonymous reviewer(s) for their contribution to the peer review of this work. Peer review reports are available.

Reprints and permissions information is available at http://www.nature.com/reprints.

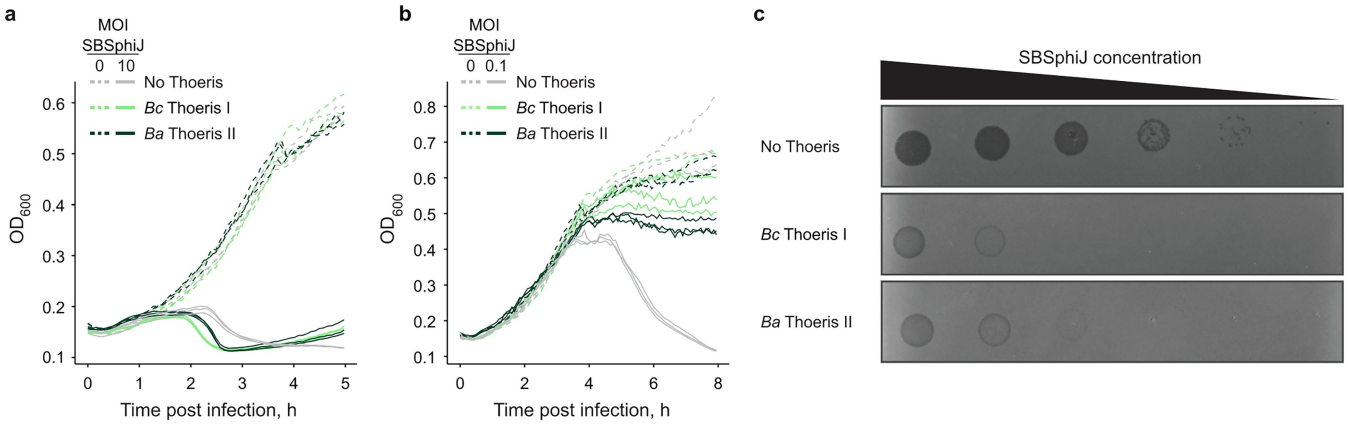

Extended Data Fig. 1 | Both type I and type II Thoeris systems protect via abortive infection. a, Growth curves of Thoeris-expressing and control cultures with and without infection by phage SBSphiJ at an MOI of 10. Data from three replicates are presented as individual curves. OD_{600}, optical density at 600 nm. **b**, Same as in panel A, but with cells infected at MOI of 0.1. **c**, A representative plaque assay showing that both type I and type II Thoeris systems protect from phage SBSphiJ. Shown are tenfold serial dilution plaque assays with phage SBSphiJ. Representative of three replicates.

```
MoTad2     1  ------MDSLNFGKALEALKEGKKVSREGWNGKGMFAYYVPGGVYK---SQT-DVIKNTF 50
TmTad2     1  MLKIREEKKMNFGKALEEVKKGKKTARKGWNGKNQYIELATAISYVNVNGELVNCNHDAI 60
CcTad2     1  ---------MNFGQALEAVKAGAKIYRQGWNGKGQFVIKAGGYTVNEPRPGS-DYAKAGI 50
                      :***:*** :* * *  *:*****. :   . .          :  :  :

MoTad2    51  GEEVKYRPYLALKTVDN-DIATWTPSVSDILAEDWNIVE- 88
TmTad2    61  GN-----KAIAFVG-TSGVQIGWLASQADMLAEDWEVVG- 93
CcTad2    51  AGEFTIQPHLDLKNAQGQMQPGWVPSQGDLFAEDWIAESP 90
              .        : :    .     *  * .*::****
```

Extended Data Fig. 2 | Multiple sequence alignment of *Mo*Tad2, *Tm*Tad2 and *Cc*Tad2. Multiple sequence alignment was performed using the HHpred server[59].

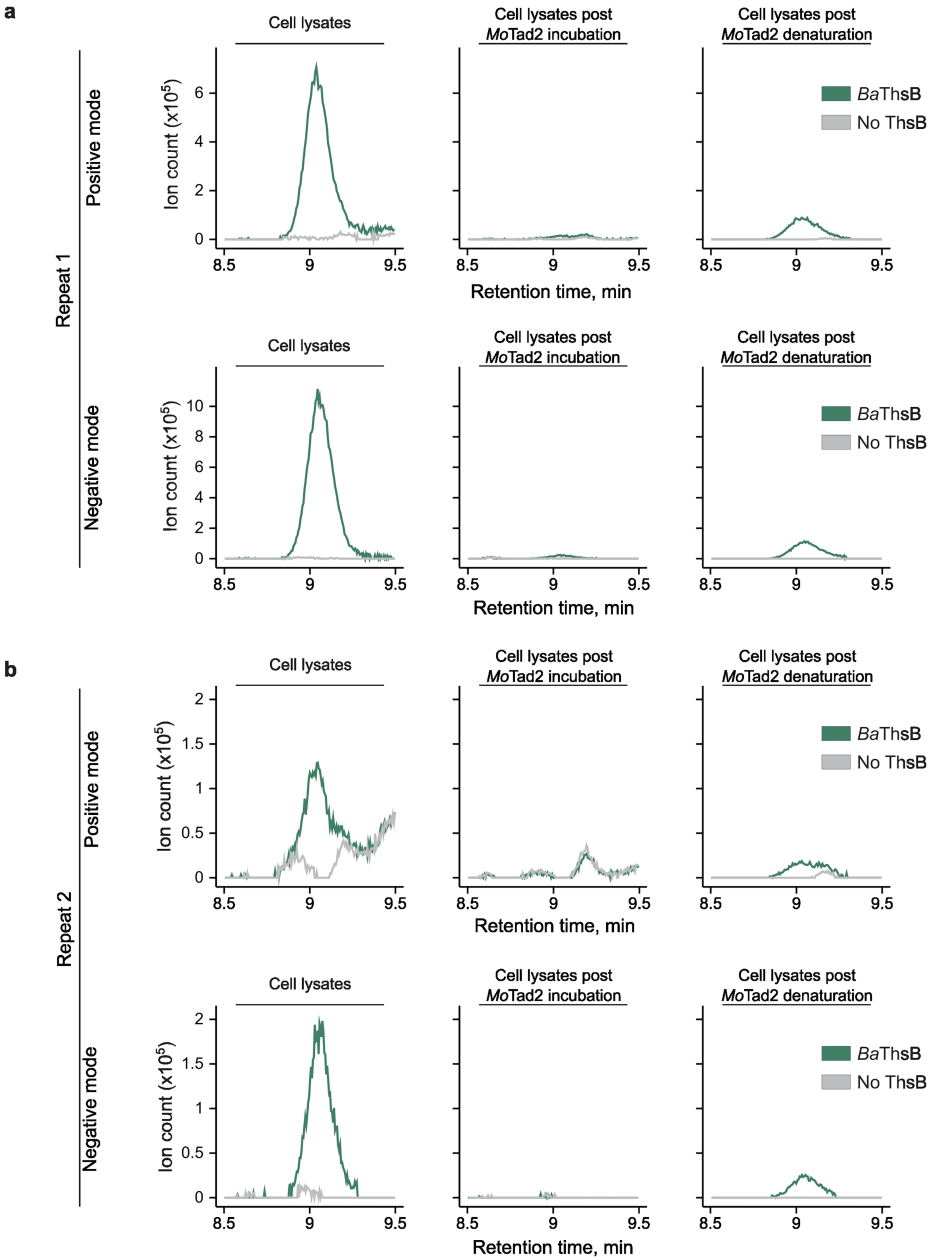

Extended Data Fig. 3 | Purified *Mo*Tad2 protein binds type II Thoeris-derived signaling molecule. a, **b**, Two repeats of the mass spectrometry (MS) analysis shown in Fig. 3a, analyzed in both positive and negative modes. Cells expressing *Ba*ThsB or control cells that express GFP instead were infected with phage SBSphiJ at MOI = 10. After 120 min the cells were lysed and lysates filtered, then incubated with purified *Mo*Tad2. The lysates prior to and post-incubation with *Mo*Tad2, or after denaturation of *Mo*Tad2, were analyzed by mass spectrometry (MS). Masses visualized in positive mode are in the m/z range of 697.1262 – 697.1462 with a retention time of 8.5 – 9.5 min. Masses visualized in a negative mode in S3 are in the m/z range of 695.1153 – 695.1353 with a retention time of 8.5 – 9.5 min. Extracted mass chromatograms of ions with an m/z value of 697.1374 and retention time of 9.04 min are presented in positive mode. In negative mode, extracted mass chromatograms of ions with an m/z value of 695.1251 are presented. Data in panel a are the same data presented in Fig. 3a.

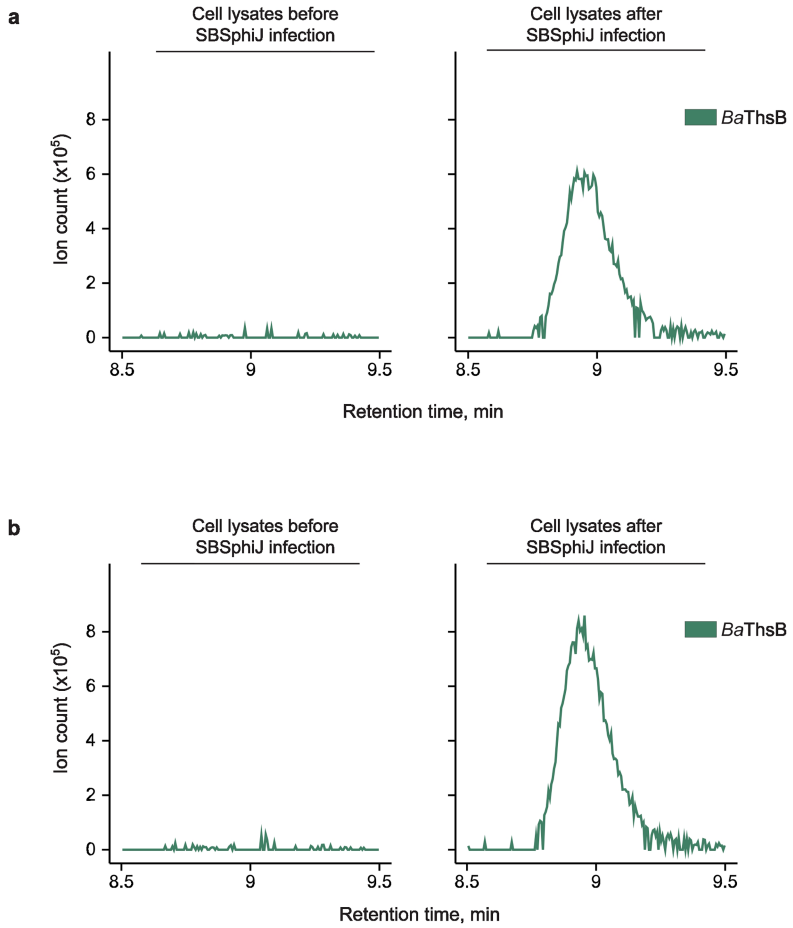

Extended Data Fig. 4 | His-ADPR is produced by *Ba*ThsB only in response to phage infection. a, b Two repeats of the mass spectrometry analysis of the level of His-ADPR molecules produced by *Ba*ThsB before and after infection with phage SBSphiJ. A 50 mL culture of cells expressing *Ba*ThsB were collected before infection and 120 min after infection with phage SBSphiJ at MOI = 10. Expression of *Ba*ThsB was induced by 100 µM IPTG. The cells were lysed and lysates were filtered and analyzed by untargeted mass spectrometry. Shown are masses recorded in positive ionization mode in the m/z range of 3 PPM around the theoretical m/z of His-ADPR with a retention time of 8.5 – 9.5.

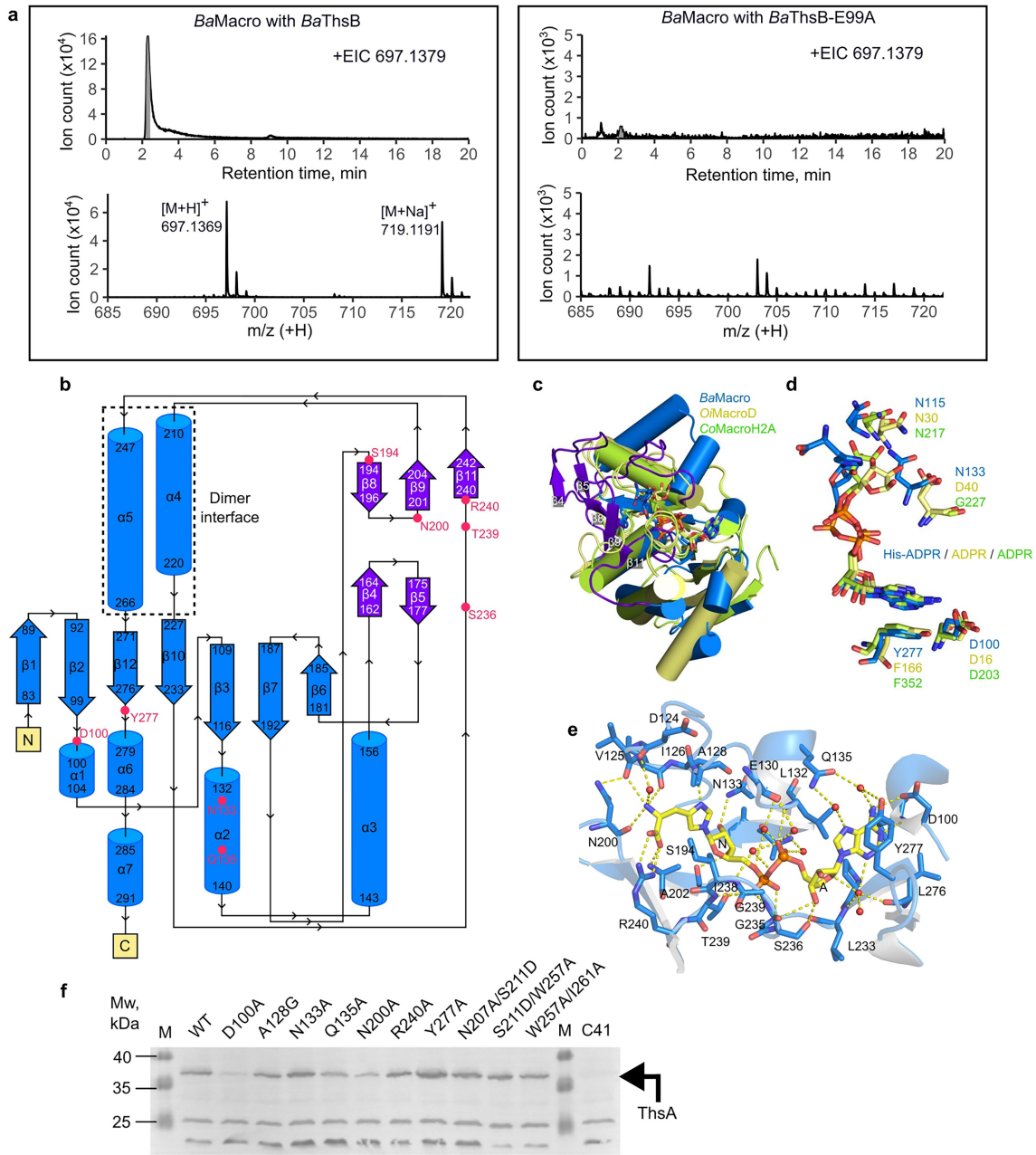

Extended Data Fig. 5 | Structural features of the *Ba*Macro domain. a, LC-MS analysis of *Ba*Macro protein purified from the cells expressing *Ba*ThsB protein or its active site E99A mutant. Shown are the extracted mass chromatograms (EIC) of ions with an m/z value of 697.1374 corresponding to His-ADPR. The mass spectrogram is shown for the gray-colored area in the EIC. Theoretical m/z of His-ADPR ions: $[M + H]^+$ 697.1374, $[M+Na]^+$ 719.1198. **b**, Topology diagram of *Ba*Macro domain structure. Residues that make side-chain contacts to the ligand are marked by red circles. **c**, Superposition of the *Ba*Macro domain (blue) with an ADPR-bound type *Oi*MacroD domain of bacterium *Oceanobacillus iheyensis* (yellow, PDB ID 5LAU, Dali Z-score 15.3, r.m.s.d. 2.8 Å^2 over 168 aligned atoms, 17% identity)[18] and MacroH2A-like macrodomain from *Capsaspora owczarzaki Co*MacroH2A (green, PDB ID 7NY7, Dali Z-score 13.7, r.m.s.d. 2.7 Å^2 over 152 aligned atoms, 13% identity)[19]. The *Ba*Macro domain possesses longer loops near the binding pocket (colored purple). In b, c Unique *Ba*ThsA elements: a β hairpin (strands β4 and β5) and a small beta-sheet (strands β8, 9, 11) are marked. **d**, Conserved residues of the ligand binding pockets of the *Ba*Macro (blue), *Oi*MacroD (yellow) and *Co*MacroH2A (green). Ligand molecules bound in the binding pocket are colored respectively. *Oi*MacroD catalytic aspartate D40 is not conserved in *Ba*ThsA and *Co*MacroH2A. **e**, Detailed view of the *Ba*ThsA residues interacting with His-ADPR. Yellow dashed lines denote hydrogen bonding interactions. A and N marks A- and N-ribose, respectively. **f**, Western blot analysis of cell lysates from cells expressing *Ba*ThsA and its mutants. M - PageRuler™ Prestained Protein Ladder, C41 - *E. coli* C41 cell lysate. The arrow indicates the bands containing *Ba*ThsA (Mw 36.558 kDa). Shown is a cropped image of one of two replicates (provided in Supplementary Fig. 1).

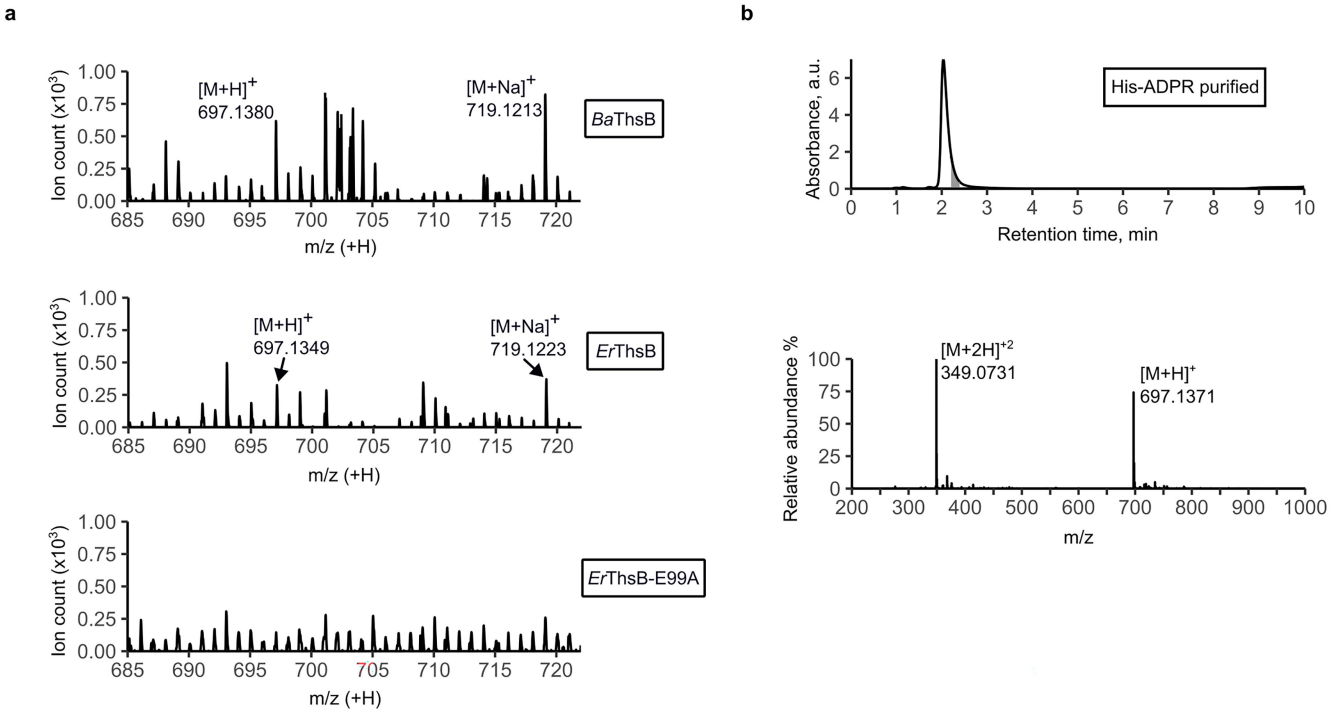

Extended Data Fig. 6 | LC-MS analysis of His-ADPR in vitro synthesis reactions and purified compound. a, LC-MS analysis of ThsB (from *B. amyloliquefaciens* Y2 and *E. rectale* ATCC 33656) in vitro reactions. Mass spectrograms indicate the presence of His-ADPR ions (theoretical m/z values $[M + H]^+$ 697.1374, $[M+Na]^+$ 719.1198). No His-ADPR is present in the *Er*ThsB-E99A sample. **b**, LC-MS analysis of the purified His-ADPR. His-ADPR molecule was obtained from the *Ba*Macro domain preparation by denaturing the protein and purifying His-ADPR by HPLC. Shown is the UV chromatogram and mass spectrogram of the interval specified by the gray area. Theoretical masses of His-ADPR ions: $[M + H]^+$ 697.1374, $[M + 2H]^{+2}$ 349.0726.

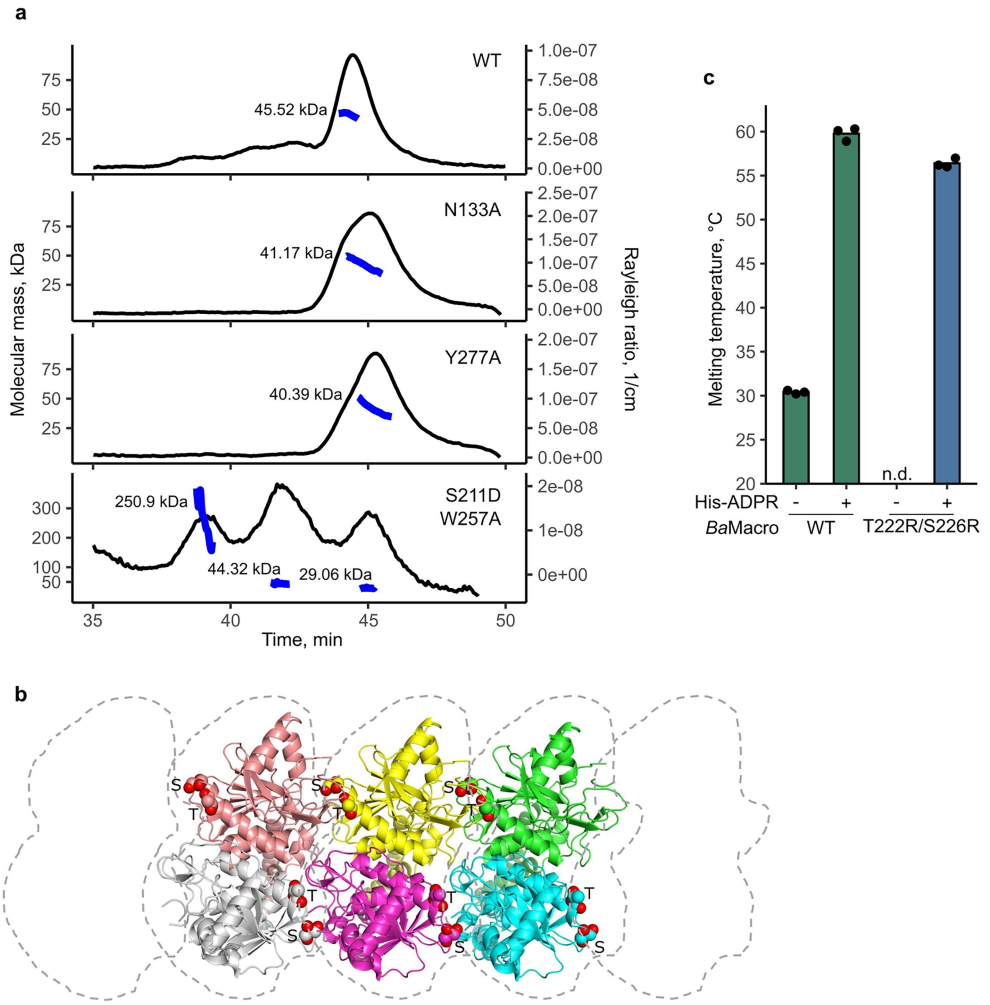

Extended Data Fig. 7 | Analysis of *Ba*Macro mutants. a, SEC-MALS analysis of the purified *Ba*Macro and its mutants. Blue lines indicate molecular weight estimates. Calculated *Ba*Macro Mw: monomer 28.914 kDa, dimer 57.829 kDa. **b**, Predicted oligomer contacts in the *Ba*ThsA AlphaFold 3 model. Subunits are shown in different colors, dimers are marked by dashed lines. Interface residues T222 (T) and S226 (S) are shown in sphere representation. **c**, Protein melting data showing Tm values of apo- and His-ADPR bound *Ba*Macro domain and its T222R/S226R mutant. Tm value of apo T222R/S226R mutant could not be determined (n.d.). Bars represent an average of three replicates with individual data points overlaid.

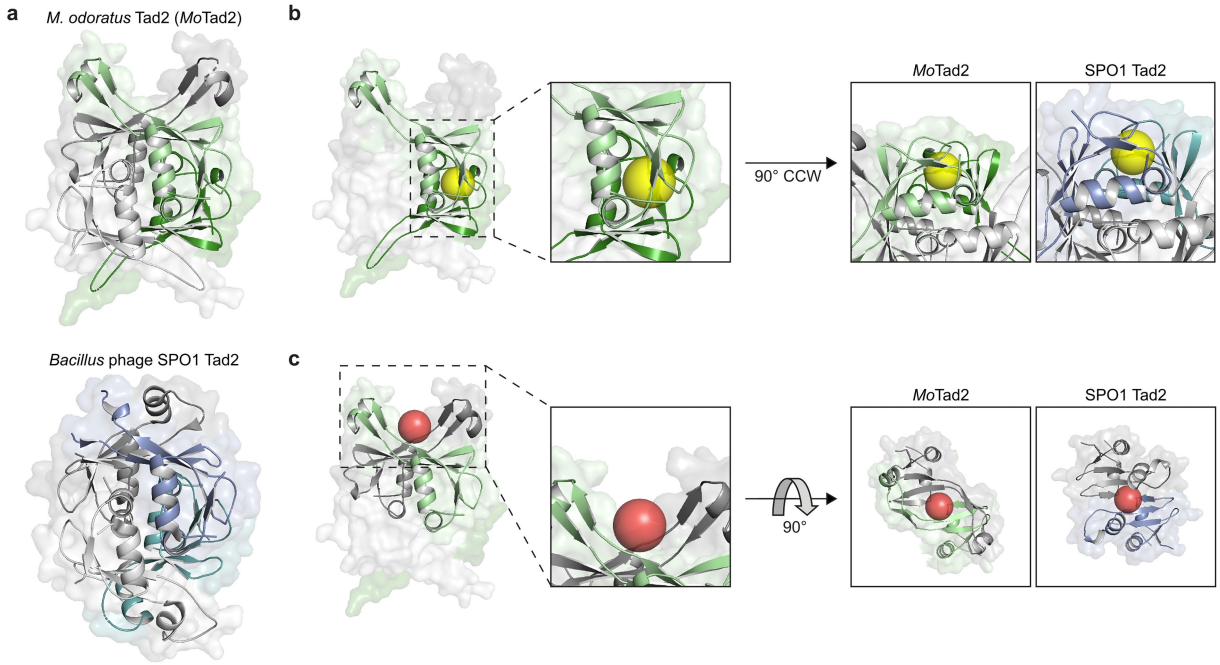

Extended Data Fig. 8 | Structural features of apo *Mo*Tad2 and comparison with SPO1 Tad2. a, Structure of apo *Mo*Tad2 tetramer (top) and *Bacillus* phage SPO1 Tad2[23] (PDB ID 8SMF, bottom). **b**, Comparison of the canonical gcADPR binding site observed in the structures of *Mo*Tad2 and SPO1 Tad2, with a yellow sphere modeled in the cavity. **c**, Comparison of the putative second binding pocket observed in *Mo*Tad2 and SPO1 Tad2, with a red sphere modeled centrally in the cavity. Mutated *Mo*Tad2 pockets residues (see, Fig. 4d) are shown in stick representation in the inlets of b and c.

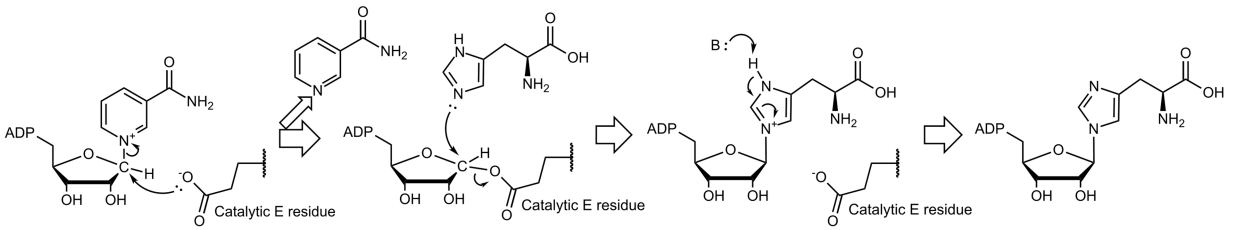

Extended Data Fig. 9 | Proposed His-ADPR synthesis by ThsB reaction mechanism. Specified catalytic glutamate (E) residue corresponds to E99A in *Ba*ThsB and *Er*ThsB. We propose that ThsB acts via a double-displacement catalytic mechanism suggested for the TIR domain of SARM1[25], in which a covalent intermediate of the glycosyl-enzyme complex with the catalytic glutamate residue is formed.

Extended Data Table 1 | Summary of data collection and refinement statistics

	*Ba*Macro* His-ADPR bound (8R66)	*Mo*Tad2 apo* (8V3E)	*Mo*Tad2 His-ADPR bound (9EIB)
Data collection			
Space group	C 1 2 1	H 3 2	P 63 2 2
Cell dimensions			
a, *b*, *c* (Å)	140.30, 71.06, 51.96	93.21, 93.21, 235.55	92.36, 92.51, 77.84
α, β, γ (°)	90, 96.78, 90	90.00, 90.00, 120.00	90.03, 90.01, 119.94
Resolution (Å)	69.7-2.23 (2.34-2.23)	47.57–2.39 (2.48–2.39)	30.34–1.67 (1.78–1.67)
R_{merge}	0.057 (0.366)	0.094 (0.177)	0.200 (3.153)
R_{pim}	0.025 (0.198)	0.039 (0.071)	0.032 (0.530)
$I / \sigma I$	9.0 (1.8)	11.9 (6.5)	15.0 (1.6)
Completeness (%)	97.1 (79.9)	99.0 (95.2)	94.7 (58.9)
Redundancy	6.5 (4.4)	6.9 (6.6)	38.9 (35.9)
Refinement			
Resolution (Å)	69.7-2.23	45.57–2.39	30.34–1.67
No. reflections			
Total	159305	109160	646995
Unique	24248	15786	16652
Free	2454	1507	855
R_{work} / R_{free}	0.186 / 0.226	0.227 / 0.273	0.208/0.238
No. atoms			
Protein	3435 (2 copies)	2503 (4 copies)	1383 (2 copies)
Ligand/ion	97	–	92
Water	82	206	162
B-factors			
Protein	55.62	25.61	31.64
Ligand/ion	49.93	–	18.18
Water	52.44	26.13	36.13
R.m.s. deviations			
Bond lengths (Å)	0.003	0.002	0.007
Bond angles (°)	0.598	0.440	1.010

*Dataset was collected from an individual crystal
Values in parentheses are for the highest-resolution shell.

nature portfolio

Corresponding author(s): Giedre Tamulaitiene, Rotem Sorek, Philip J. Kranzusch

Last updated by author(s): Mar 6, 2025

Reporting Summary

Nature Portfolio wishes to improve the reproducibility of the work that we publish. This form provides structure for consistency and transparency in reporting. For further information on Nature Portfolio policies, see our Editorial Policies and the Editorial Policy Checklist.

Statistics

For all statistical analyses, confirm that the following items are present in the figure legend, table legend, main text, or Methods section.

n/a	Confirmed
☐	☒ The exact sample size (*n*) for each experimental group/condition, given as a discrete number and unit of measurement
☐	☒ A statement on whether measurements were taken from distinct samples or whether the same sample was measured repeatedly
☒	☐ The statistical test(s) used AND whether they are one- or two-sided *Only common tests should be described solely by name; describe more complex techniques in the Methods section.*
☒	☐ A description of all covariates tested
☒	☐ A description of any assumptions or corrections, such as tests of normality and adjustment for multiple comparisons
☐	☒ A full description of the statistical parameters including central tendency (e.g. means) or other basic estimates (e.g. regression coefficient) AND variation (e.g. standard deviation) or associated estimates of uncertainty (e.g. confidence intervals)
☒	☐ For null hypothesis testing, the test statistic (e.g. *F*, *t*, *r*) with confidence intervals, effect sizes, degrees of freedom and *P* value noted *Give P values as exact values whenever suitable.*
☒	☐ For Bayesian analysis, information on the choice of priors and Markov chain Monte Carlo settings
☒	☐ For hierarchical and complex designs, identification of the appropriate level for tests and full reporting of outcomes
☒	☐ Estimates of effect sizes (e.g. Cohen's *d*, Pearson's *r*), indicating how they were calculated

Our web collection on statistics for biologists contains articles on many of the points above.

Software and code

Policy information about availability of computer code

Data collection	X-ray diffraction data were collected at the beamline P13 operated by EMBL Hamburg at the PETRA III storage ring using mxCuBE software v. 1 (DESY, Hamburg, Germany) and at the Northeastern Collaborative Access Team beamlines 24-ID-C and 24-ID-E (P30 GM124165) using RAPD, 17-ID-2 (FMX) using blueskey v1.6.7. DLS measurements were performed with a Zetasizer µV photometer (Malvern Panalytical) using Zetasizer Software (v6.20). LC-MS analysis was performed using Q Exactive Plus Orbitrap™ (Thermo Fisher Scientific) and HPLC system 1290 Infinity (Agilent Technologies) coupled to mass analyser 6520 Accurate Mass Q-TOF LC/MS (Agilent Technologies), data acquisition was performed on MassHunter and QTOF Acquisition Software (B.02.01 SP1). Thermal shift assay was performed using Prometheus NT.48 (NanoTemper) with using PR. Therm Control (v2.3.1) software.
Data analysis	X-ray data analysis software: SSRL autoxds script (A. Gonzalez, Stanford SSRL), ColabFold v1.5.3, WinCoot, PyMOL (v2.3.0; v2.5.0; v2.5.4), XDS (version Mar 15, 2019), SCALA and TRUNCATE (CCP4 package 7.0.076), Phaser (2.8.0), Phenix (phenix-1.20.1-4487; 1.21.1), Coot (0.9.7; 0.8.9.3), eLBOW (phenix-1.20.1-4487), autoPROC (10.07.2024), Aimless (0.7.9), PyMOL (v.2.3.0; v.2.5.4) DLS analysis software: Zetasizer Software (v6.20). MS analysis software: MZmine 2.5.3, MassHunter (vB.05.00, Agilent Technologies). Thermal shift data analysis software PR. Therm Control (v2.3.1).

For manuscripts utilizing custom algorithms or software that are central to the research but not yet described in published literature, software must be made available to editors and reviewers. We strongly encourage code deposition in a community repository (e.g. GitHub). See the Nature Portfolio guidelines for submitting code & software for further information.

Data

Policy information about availability of data

All manuscripts must include a data availability statement. This statement should provide the following information, where applicable:

- Accession codes, unique identifiers, or web links for publicly available datasets
- A description of any restrictions on data availability
- For clinical datasets or third party data, please ensure that the statement adheres to our policy

All data are available in the Article and the Supplementary Material. Strains of bacteria and phages and plasmid maps of the constructs used for the experiments are attached as Supplementary Files. The atomic coordinates and structure factors have been deposited in the Protein Data Bank under accession codes 8V3E (ModTad2), 9EIB (His-ADPR bound ModTad2) and 8R66 (His-ADPR bound Macroamylo). The crystal structures in Extended Fig. 5c,d (5LAU, 7NY7), Extended Fig. 8 (8SMF) are publicly available from Protein Data Bank. Source data for Fig. 1-4, Extended Data Fig. 1,3-7 are provided with this paper.

Research involving human participants, their data, or biological material

Policy information about studies with human participants or human data. See also policy information about sex, gender (identity/presentation), and sexual orientation and race, ethnicity and racism.

Reporting on sex and gender	not applicable
Reporting on race, ethnicity, or other socially relevant groupings	not applicable
Population characteristics	not applicable
Recruitment	not applicable
Ethics oversight	not applicable

Note that full information on the approval of the study protocol must also be provided in the manuscript.

Field-specific reporting

Please select the one below that is the best fit for your research. If you are not sure, read the appropriate sections before making your selection.

☒ Life sciences ☐ Behavioural & social sciences ☐ Ecological, evolutionary & environmental sciences

For a reference copy of the document with all sections, see nature.com/documents/nr-reporting-summary-flat.pdf

Life sciences study design

All studies must disclose on these points even when the disclosure is negative.

Sample size	No sample size calculations were performed since it is not relevant to structural, biochemical or phage challenge experiments. X-ray dataset size was determined by the crystal diffraction resolution. 2-3 independent replicates of biochemical and in vivo experiments were performed as it is described in the Fig. legends/Methods.
Data exclusions	No data were excluded
Replication	Reproducibility was ensured by repeating most of the experiments independently at least 3 times. All 3 replications were successful.
Randomization	Not relevant to this study as there are no animal nor human experiments, and the experimental outcome does not depend on the order in which samples were analyzed in the experiments.
Blinding	Not relevant to this study as there are no animal nor human experiments, and the knowledge of the order or identity of a sample does not change the experimental outcome.

Reporting for specific materials, systems and methods

We require information from authors about some types of materials, experimental systems and methods used in many studies. Here, indicate whether each material, system or method listed is relevant to your study. If you are not sure if a list item applies to your research, read the appropriate section before selecting a response.

Materials & experimental systems

n/a	Involved in the study
☒	☐ Antibodies
☒	☐ Eukaryotic cell lines
☒	☐ Palaeontology and archaeology
☒	☐ Animals and other organisms
☒	☐ Clinical data
☒	☐ Dual use research of concern
☒	☐ Plants

Methods

n/a	Involved in the study
☒	☐ ChIP-seq
☒	☐ Flow cytometry
☒	☐ MRI-based neuroimaging

Plants

Seed stocks	not applicable
Novel plant genotypes	not applicable
Authentication	not applicable